











# Improved photometric redshift estimations through self-organising map-based data augmentation

Yun-Hao Zhang (张云皓)<sup>1,2\*</sup> Joe Zuntz<sup>1</sup> Irene Moskowit<sup>3</sup> Eric Gawiser<sup>3</sup> Konrad Kuijken<sup>2</sup>  
Marika Asgari<sup>4</sup> Henk Hoekstra<sup>2</sup> Alex I. Malz<sup>5,6</sup> Ziang Yan (颜子昂)<sup>7</sup> Tianqing Zhang<sup>8</sup>  
and The LSST Dark Energy Science Collaboration

<sup>1</sup> Institute for Astronomy, University of Edinburgh, Royal Observatory, Blackford Hill, Edinburgh, EH9 3HJ, The United Kingdom

<sup>2</sup> Leiden Observatory, Leiden University, Einsteinweg 55, 2333 CC, Leiden, The Netherlands

<sup>3</sup> Department of Physics and Astronomy, Rutgers, The State University of New Jersey, Piscataway, NJ 08854, The U.S.A.

<sup>4</sup> School of Mathematics, Statistics and Physics, Newcastle University, Herschel Building, NE1 7RU, Newcastle-upon-Tyne, The United Kingdom

<sup>5</sup> LSST Interdisciplinary Network for Collaboration and Computing Frameworks, 933 N. Cherry Avenue, Tucson, AZ 85721, The U.S.A.

<sup>6</sup> McWilliams Center for Cosmology and Astrophysics, Department of Physics, Carnegie Mellon University, Pittsburgh, PA 15213, The U.S.A.

<sup>7</sup> Ruhr University Bochum, Astronomical Institute (AIRUB), German Centre for Cosmological Lensing, 44780 Bochum, Germany

<sup>8</sup> Department of Physics and Astronomy and PITT PACC, University of Pittsburgh, Pittsburgh, PA 15260, The U.S.A.

Accepted XXX. Received YYY; in original form ZZZ

## ABSTRACT

We introduce a framework for the enhanced estimation of photometric redshifts using Self-Organising Maps (SOMs). Our method projects galaxy Spectral Energy Distributions (SEDs) onto a two-dimensional map, identifying regions that are sparsely sampled by existing spectroscopic observations. These under-sampled areas are then augmented with simulated galaxies, yielding a more representative spectroscopic training dataset. To assess the efficacy of this SOM-based data augmentation in the context of the forthcoming Legacy Survey of Space and Time (LSST), we employ mock galaxy catalogues from the OpenUniverse2024 project and generate synthetic datasets that mimic the expected photometric selections of LSST after one (Y1) and ten (Y10) years of observation. We construct 501 degraded realisations by sampling galaxy colours, magnitudes, redshifts and spectroscopic success rates, in order to emulate the compilation of a wide array of realistic spectroscopic surveys. Augmenting the degraded mock datasets with simulated galaxies from the independent CosmoDC2 catalogues has markedly improved the performance of our photometric redshift estimates compared to models lacking this augmentation, particularly for high-redshift galaxies ( $z_{\text{true}} \geq 1.5$ ). This improvement is manifested in notably reduced systematic biases and a decrease in catastrophic failures by up to approximately a factor of 2, along with a reduction in information loss in the conditional density estimations. These results underscore the effectiveness of SOM-based augmentation in refining photometric redshift estimation, thereby enabling more robust analyses in cosmology and astrophysics for the NSF-DOE Vera C. Rubin Observatory.

**Key words:** galaxies: distances and redshifts – methods: statistical – cosmology: large-scale structure of Universe

## 1 INTRODUCTION

Cosmological redshift underpins myriad applications in modern astronomy. Accurate redshift estimates permit the conversion of observed magnitudes of distant galaxies into intrinsic luminosities, allowing studies of the galaxy luminosity function (e.g. [Schechter 1976](#); [Finkelstein et al. 2015](#); [Bouwens et al. 2023](#)), the evolution of galaxy size and morphology across cosmic epochs (e.g. [Conselice 2014](#); [Shibuya et al. 2015](#)), and scaling relations between galaxy stellar masses and properties of their interstellar medium (e.g. [Kennicutt 1998](#); [Tremonti et al. 2004](#)), central supermassive black holes (e.g. [Kormendy & Ho 2013](#)), and host haloes (e.g. [Behroozi et al. 2013](#); [Wechsler & Tinker 2018](#)).

In cosmology, Type Ia supernova host galaxy redshifts provided

the first direct evidence of the accelerating expansion of the Universe ([Riess et al. 1998](#); [Perlmutter et al. 1999](#)). Baryon Acoustic Oscillations (BAOs), measured from galaxy clustering, act as a standard ruler for cosmic distances ([Eisenstein et al. 2005](#)), while large-scale structure surveys map the growth of density fluctuations ([Peebles 1980](#); [Springel et al. 2006](#)). The weak gravitational lensing of distant galaxies ([Tyson et al. 1990](#); [Kaiser 1998](#); [Bartelmann & Schneider 2001](#)) enables the reconstruction of the matter distribution and serves as a sensitive probe of dark energy through cosmic-shear tomography ([Kilbinger 2015](#)). Collectively, these observables demonstrate how cosmological redshift is the keystone linking local galaxy properties to the geometry and dynamics of the Universe, and a critical underpinning of the concordance  $\Lambda$ CDM model.

Recent wide-field imaging surveys offer multi-wavelength photometry for hundreds of millions of galaxies, such as the Kilo-Degree

\* YunHao.Zhang@ed.ac.uk

Survey (KiDS<sup>1</sup>; Wright et al. 2024), the Dark Energy Survey (DES<sup>2</sup>; Bechtol et al. 2025), and the Hyper Suprime-Cam Survey (HSC<sup>3</sup>; Li et al. 2022). Nonetheless, acquiring precise redshifts using spectroscopy for such extensive samples remains exceedingly resource-demanding. As a result, studies on large-scale structures and galaxy evolution are increasingly dependent on photometric redshift methods, which estimate redshifts from broadband flux observations, a technique initially proposed by Koo (1985); Loh & Spillar (1986).

Next-generation facilities – including the NSF-DOE Vera C. Rubin Observatory (Rubin<sup>4</sup>; LSST Science Collaboration et al. 2009), the Euclid mission (Euclid<sup>5</sup>; Euclid Collaboration et al. 2025), the Nancy Grace Roman Space Telescope (Roman<sup>6</sup>; Spergel et al. 2015) and the China Space Station Telescope (CSST<sup>7</sup>; Gong et al. 2019) – will deliver unprecedented imaging depth and sky coverage. Exploiting their full cosmological potential to probe dark matter and dark energy, however, demands exceptional control of systematic uncertainties, especially in photometric redshift performance (Mandelbaum 2018).

In recent decades, numerous techniques for estimating photometric redshifts have been developed and are generally classified into two categories based on the type of data and the priors used during inference, as reviewed in Newman & Gruen (2022). Comprehensive descriptions of most of these techniques are available through the Redshift Assessment Infrastructure Layers (RAIL<sup>8</sup>; The RAIL Team et al. 2025) platform for Legacy Survey of Space and Time (LSST) Dark Energy Science Collaboration (DESC). Specifically, the most traditional approach, template fitting, matches observed broadband photometry to libraries of galaxy Spectral Energy Distribution (SED) templates, using software packages such as LePhare (Arnouts et al. 1999; Ilbert et al. 2006), BPZ (Benítez 2000; Coe et al. 2006), ZEBRA (Feldmann et al. 2006), EAZY (Brammer et al. 2008), and DELIGHT (Leistedt & Hogg 2017). By incorporating stellar population synthesis models, template fitting can recover redshift posteriors from noisy magnitude measurements; however, the limited completeness of template sets and potential biases in the adopted priors can introduce systematic errors and constrain the ultimate accuracy of the estimates (e.g. Hildebrandt et al. 2010; Dahlen et al. 2013).

Conversely, a variety of machine-learning algorithms have been devised to characterise the complex relationship between galaxy broadband SEDs and redshifts, utilising galaxies with known redshifts. These include artificial neural networks (ANNz; Collister & Lahav 2004; Sadeh et al. 2016), decision trees with random forest techniques, Gaussian processes (GPz; Almosallam et al. 2016), the quasi-Newton algorithm (MLPQNA; Cavuoti et al. 2012), hybrid density estimation (METAPHOR; Cavuoti et al. 2017), boosted decision trees combined with basis function decomposition (FlexZBoost; Izbicki & Lee 2017; Dalmaso et al. 2020; Schmidt et al. 2020), the normalising flow algorithm (PZFlow; Crenshaw et al. 2024), and stratified learning (StratLearn-z; Revsbech et al. 2018; Autenrieth et al. 2024; Moretti et al. 2025), and

These data-driven approaches rely on training samples with high completeness and precisely measured redshifts, typically drawn from wide-area spectroscopic surveys such as the Sloan Digital Sky Sur-

vey (SDSS<sup>9</sup>; York et al. 2000), the Two-degree Field Galaxy Redshift Survey (2DFGRS<sup>10</sup>; Colless et al. 2001) and the Galaxy And Mass Assembly survey (GAMA<sup>11</sup>; Driver et al. 2011), as well as deep spectroscopic programmes (e.g. zCOSMOS; Lilly et al. 2007, DEEP2; Newman et al. 2013, VIPERS; Guzzo et al. 2014). Narrow-band imaging campaigns (e.g. J-PAS<sup>12</sup>; Benítez et al. 2015, PAUS<sup>13</sup>; Daza-Perilla et al. 2025) extend this reach to fainter magnitudes and higher redshifts. New and forthcoming facilities – among them the Dark Energy Spectroscopic Instrument (DESI<sup>14</sup>; DESI Collaboration et al. 2024), the Subaru Prime Focus Spectrograph (PFS<sup>15</sup>; Takada et al. 2014), the 4-metre Multi-Object Spectroscopic Telescope (4MOST<sup>16</sup>; Walcher et al. 2016) and William Herschel Telescope Enhanced Area Velocity Explorer (WEAVE<sup>17</sup>; Jin et al. 2024) – promise substantially improved spectroscopic completeness, thereby enhancing the training and accuracy of machine-learning photometric-redshift estimators.

Nevertheless, spectroscopic samples remain subject to magnitude limits and exhibit uneven coverage in redshift-colour space, resulting in non-representative training datasets and inducing selection biases (Hartley et al. 2020; Wright et al. 2020). Spectroscopic misidentifications and catalogue mismatches further introduce systematic offsets in point estimates and distort the shapes of posterior redshift distributions (Masters et al. 2015). Moreover, degeneracies in galaxy SEDs and redshift-colour ambiguities exacerbate these biases. Mitigating these challenges therefore demands robust statistical frameworks, truly representative calibration samples and explicit correction schemes that account for spectroscopic incompleteness.

To address these limitations, an alternative method introduced by (Moskowitz et al. 2024) utilises synthetic mock galaxy catalogues to supplement missing galaxy SEDs, thereby providing more representative datasets for training machine learning methods to estimate photometric redshifts. This requires a careful understanding of the realism of the supplemental catalogue, but was shown to provide significant improvements, particularly in high-redshift estimation where the training dataset is least representative.

In this study, we extend this approach by employing the Self-Organising Map (SOM) machine learning algorithm to identify regions with insufficient spectroscopic redshift coverage, and preferentially augment those regions. This facilitates a more effective augmentation of simulated galaxies, resulting in enhanced accuracy in photometric redshift estimates. We also introduce controlled variations in the degradation and augmentation protocols to quantify the impact of differing spectroscopic selection functions, and to evaluate photometric redshift performance under both one-year (Y1) and ten-year (Y10) survey depth of LSST.

This work centres on generating realistic photometric and spectroscopic datasets of galaxies for LSST cosmological analyses, showcasing how SOM-based data augmentation improves the photometric redshift estimates for individual galaxies. In a forthcoming study (Zhang et al. in preparation), we establish the tomographic binning

<sup>1</sup> <https://kids.strw.leidenuniv.nl>

<sup>2</sup> <https://www.darkenergysurvey.org>

<sup>3</sup> <https://hsc.mtk.nao.ac.jp/ssp/>

<sup>4</sup> <https://rubinobservatory.org>

<sup>5</sup> <https://www.cosmos.esa.int/web/euclid>

<sup>6</sup> <https://roman.gsfc.nasa.gov>

<sup>7</sup> <http://www.bao.ac.cn/csst/>

<sup>8</sup> <https://github.com/LSSTDESC/rail>

<sup>9</sup> <https://www.sdss.org>

<sup>10</sup> <http://www.2dfgrs.net>

<sup>11</sup> <https://www.gama-survey.org>

<sup>12</sup> <https://www.j-pas.org>

<sup>13</sup> <https://www.paus-survey.org>

<sup>14</sup> <https://www.desi.lbl.gov>

<sup>15</sup> <https://pfs.ipmu.jp>

<sup>16</sup> <https://www.4most.eu/cms/home/>

<sup>17</sup> <https://www.ing.iac.es/astronomy/instruments/weave/weaveinst.html>

of galaxy samples and further develop this method to calibrate the ensemble redshift distributions for each tomography.

The structure of the paper is as follows: Section 2 provides a review of the mock galaxy catalogues; Section 3 outlines our photometric and spectroscopic sample selection and augmentation process; Section 4 explains our photometric redshift modelling; Section 5 evaluates the precision achieved; and Section 6 concludes with a summary of our findings and presents opportunities for future research.

## 2 MOCK GALAXY CATALOGUE

To ensure realism and utility, tests of the data-augmentation method using simulated galaxies must employ catalogues that exhibit authentic differences. In practice, the discrepancy between the real observation and one simulation should be comparable to that between two distinct simulations employed in our study. If the mocks were identical, augmentation would trivially succeed but offer no insight into its effectiveness in real analyses; if they were unrealistically different, augmentation would fail outright.

In this section, we outline the key features of the two input mock galaxy catalogues, CosmoDC2 and OpenUniverse2024, that serve as the starting points for our data manipulation and analysis. The OpenUniverse2024 catalogue is utilised to emulate the properties of galaxies expected in forthcoming LSST observations, whereas CosmoDC2 is used here solely for data augmentation. Our selected catalogues closely resemble actual observations; nevertheless, they exhibit differences, offering an appropriate testing environment for the intended application of the method. This variation effectively represents the systematic discrepancies between synthetic catalogues and real observations, thereby reproducing a significant source of bias in photometric-redshift estimation through data augmentation.

### 2.1 CosmoDC2

The CosmoDC2 catalogue (Korytov et al. 2019) is a comprehensive, purpose-designed resource for *Rubin* cosmology. This constitutes the foundation of the second Data Challenge (DC2; LSST Dark Energy Science Collaboration et al. 2021) conducted by the LSST DESC. Derived from the Outer Rim N-body simulation (Heitmann et al. 2019), it models a cosmic volume of  $(4.225 \text{ Gpc})^3$  using over a trillion  $10^{240^3}$  particles, each with a mass of  $2.6 \times 10^9 M_\odot$ . The simulation suite comprises roughly 100 temporal snapshots, recorded from  $z \sim 10$  to  $z = 0$ , and was created using the Hybrid/Hardware Accelerated Cosmology Code (HACC; Habib et al. 2016 on the IBM BG/Q system Mira at the Argonne Leadership Computing Facility (ALCF<sup>18</sup>).

To incorporate realistic galaxy properties, CosmoDC2 employs GalSampler (Hearin et al. 2020), a hybrid approach that merges semi-analytic modelling using Galacticus (Benson et al. 2012), with empirical techniques based on the UniverseMachine (Behroozi et al. 2019). This method transfers sophisticated stellar population synthesis prescriptions to cosmological simulations via halo-to-halo correspondence, incorporating more than 500 galaxy attributes, including the *Rubin* photometry in the  $u, g, r, i, z, y$  filters, morphology, halo properties, and weak lensing shear. CosmoDC2 has been validated against the scientific objectives of LSST DESC (Kovacs et al. 2022), and its simulated catalogues span over  $440 \text{ deg}^2$  of

sky up to a redshift of  $z = 3$ , reaching a magnitude depth of  $r = 28$  and supporting a broad range of scientific applications.

### 2.2 OpenUniverse2024

The OpenUniverse2024 extragalactic catalogue (OpenUniverse et al. 2025) builds upon the same Outer Rim dark-matter simulation used in CosmoDC2, but uses the differentiable DiffSky framework to populate galaxies within the same cosmological large-scale structure, with details introduced in lsstdesc-diffsky. Rather than relying on discrete merger-tree assembly histories and star-formation tracks, DiffSky utilises the auto-differentiable modules DiffMAH (Hearin et al. 2021), DiffStar (Alarcon et al. 2023), and DSPS (Hearin et al. 2023) to derive smooth, physically motivated parametrisations of mass assembly histories, star formation histories, and stellar population synthesis modelling. This approach yields robust predictions of stellar mass and star formation rates, even in poorly resolved haloes. The resulting position, lensing shear and convergence, morphological parameters, and multi-wavelength SED of each galaxy are consolidated within SkyCatalog, a unified truth-catalogue format. OpenUniverse2024 covers approximately  $110 \text{ deg}^2$  – corresponding to both the LSST Deep Drilling Fields (DDFs; Gris et al. 2024) and the Roman High-Latitude Imaging Survey (Akeson et al. 2019).

### 2.3 Comparison of catalogues

Both CosmoDC2 and OpenUniverse2024 employ galaxy SED models that have been rigorously validated against deep, multi-band survey data. Owing to its fully differentiable framework, the mock colours and number counts of OpenUniverse2024 agree with those of the COSMOS2020 survey at the per cent level (Weaver et al. 2022; Shuntov et al. 2022). Similarly, CosmoDC2 demonstrates excellent consistency in its bright, low-redshift galaxy population when evaluated with the LSST DESCQA validation suite (Mao et al. 2018).

As illustrated by the green points in Figure 1, the colour–redshift distribution of CosmoDC2 exhibits pronounced discreteness at high redshift compared to the orange points for OpenUniverse2024. This behaviour originates from its dependence on a restricted array of stellar population templates. We therefore utilise CosmoDC2 to construct our augmentation catalogues, thereby compensating for gaps in spectroscopic coverage. In a practical analysis, these augmented catalogues would likewise be simulated datasets, with their SEDs mildly differing from those in the observational datasets.

Conversely, the auto-differentiable, parameterised models utilised by OpenUniverse2024 produce smoother and more physical colour distributions, rendering it an excellent proxy for LSST-like observations. In this study, we utilise OpenUniverse2024 as the finest available alternative to the actual observational dataset expected from the forthcoming LSST.

At low redshift ( $z_{\text{true}} \lesssim 1.5$ ), both catalogues exhibit excellent agreement in the  $i - z$  and  $z - y$  colours, particularly for bright galaxies ( $i \lesssim 22.5$ ). Conversely, CosmoDC2 shows a systematic excess of redder  $u - g$  and  $g - r$  colours relative to OpenUniverse2024 especially among low-redshift ( $z_{\text{true}} \lesssim 1.5$ ) and faint galaxies ( $i \gtrsim 22.5$ ), reflecting differences in the treatment of stellar populations at the blue end of the SED. As detailed below, these offsets can be partly mitigated by weighted resampling of the CosmoDC2 galaxies to match the smoother distributions of OpenUniverse2024.

At fainter magnitudes ( $i \gtrsim 22.5$ ) and higher redshifts ( $z_{\text{true}} \gtrsim 1.5$ ), where spectroscopic calibrators are scarce, the two SED models diverge markedly, reducing their overlap. This divergence persists after

<sup>18</sup> <https://www.alcf.anl.gov>



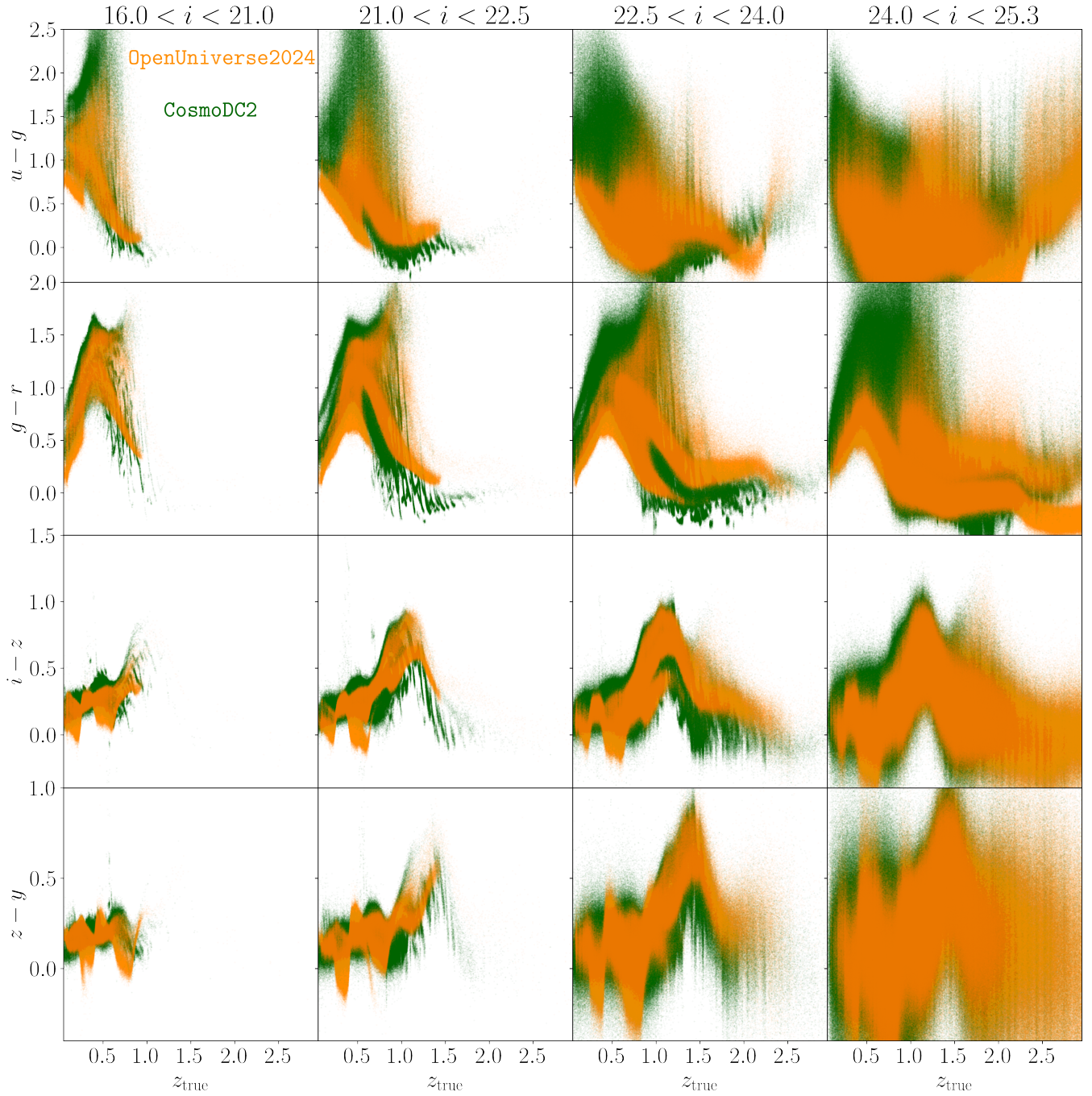


**Figure 1.** Distributions of galaxy colours as a function of true redshift are plotted in green for CosmoDC2 and orange for OpenUniverse2024, comparing their colour–redshift distributions at LSST Y10 depth. From top to bottom, the rows correspond to the  $u - g$ ,  $g - r$ ,  $i - z$  and  $z - y$  colours. Columns represent bins in  $i$ -band magnitude:  $16.0 < i < 21.0$ ,  $21.0 < i < 22.5$ ,  $22.5 < i < 24.0$  and  $24.0 < i < 25.3$ .

resampling and thus represents a significant source of systematic error in photometric-redshift modelling. Figure 1 illustrates these comparisons at LSST Y10 depth – chosen to emphasise SED differences among the faintest galaxies ( $i \gtrsim 24.0$ ) – although identical trends are evident in other observing scenarios.

### 3 DATASET CONFIGURATION

In the following, we outline our approach to utilising these advanced mock galaxy catalogues to produce several synthetic datasets. Each dataset is designed to replicate the photometric and spectroscopic selection functions of galaxy surveys for LSST photometric redshift analyses and to account for variations in selection effects. The datasets we generated are defined as follows:

- **Application:** a general LSST-like photometric sample.
- **Degradation:** a compilation of multiple spectroscopic datasets



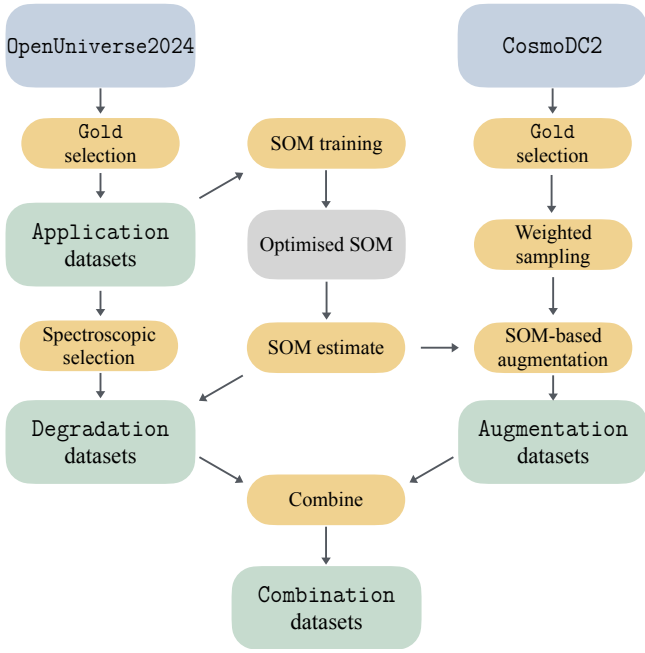


**Figure 2.** Schematic overview of the dataset generation pipeline. The diagram outlines the steps for constructing synthetic catalogues tailored to either photometric or spectroscopic selection criteria, using mock galaxies from OpenUniverse2024 and CosmoDC2.

derived from the **Application** datasets, used as part of the training sample.

- **Augmentation:** training datasets generated through simulations and added to the spectroscopic samples.
- **Combination:** complete training datasets produced through the integration of **Degradation** and **Augmentation** samples.

Figure 2 presents a schematic overview of the pipeline, illustrating the principal stages from catalogue ingestion to the production of analysis-ready datasets. In order to incorporate different systematic effects into later modelling stages, we conduct 501 experiments that produce the four catalogues. This includes one baseline experiment used for machine learning training as detailed below, and  $N = 500$  additional ones for statistical analysis.

### 3.1 Application datasets

As mentioned earlier, the OpenUniverse2024 catalogues serve as the foundation for replicating the photometric Gold selection as outlined in the LSST DESC Science Requirements Document (SRD; LSST Dark Energy Science Collaboration et al. 2018). We refer to the outcome of our Gold selection as the **Application** datasets. We then apply an unsupervised machine-learning technique for dimensionality reduction, the Self-Organising Map (SOM), to map galaxy broadband SEDs onto a two-dimensional grid, thereby facilitating subsequent analyses of spectroscopic degradation and data augmentation.

#### 3.1.1 Gold selection

Utilising the OpenUniverse2024 catalogues, the first task is to calculate realistic photometric uncertainties for observations conducted at both LSST Y1 and Y10 depths. This computation employs the publicly accessible tool ([PhotErr](#); Crenshaw et al. 2024), which

follows the survey strategy outlined in Ivezić et al. (2019). Consequently, it derives the error model for point sources as well as for extended sources characterised by the morphological properties of galaxies as described by van den Busch et al. (2020).

In the **Application** datasets, each of the 501 experiments incorporates a separate random realisation of photometric noise, achieved through a unique seed to disturb the galaxy photometry. This method guarantees the creation of statistically independent synthetic datasets that mirror observational uncertainties. When calculating the perturbed magnitudes, we manually set the fluxes at the  $1\sigma$  noise threshold for galaxies dimmer than the specified limiting magnitudes in each band, considering them as non-detections. This setting ensures that the distribution of galaxy colours remains numerically continuous, even when certain bands are not detected.

One of the key aims of the Gold selection is to pinpoint galaxies with trustworthy detections. Consequently, the **Application** datasets developed subsequent to the Gold selection embody pragmatic photometric selection standards and serve as the groundwork for subsequent photometric-redshift modelling. Therefore, in order to eliminate very faint extended sources, we require the Signal-to-Noise Ratio (SNR) obtained from the combined  $r$ - and  $i$ -band photometry, ( $\mu \equiv \text{SNR}_{i+r}$ ), to meet the condition  $\mu > 10$ . Additionally, we impose a restriction on the squared ratio of the galaxy size to the coadded point-spread function (PSF), expressed as  $\eta \equiv \left( R^{i+r} / R_{\text{PSF}}^{i+r} \right)^2$ , requiring  $\eta > 0.1$  in order to reduce contamination from unresolved point sources during practical analysis.

In addition, we exclude objects brighter than 16 in  $i$ -band to mimic the masking of bright, saturated sources, and remove galaxies fainter than 24.05 for Y1 and 25.30 for Y10, in accordance with the Gold selection defined in the LSST DESC SRD. Additionally, to capture spatial sample variance, we randomly select half of the HEALPix sky pixels from OpenUniverse2024 in each experiment.

Table 1 provides a concise overview of essential information about the baseline **Application** datasets. Differences in the supplementary experiments are minimal and thus excluded for the sake of brevity.

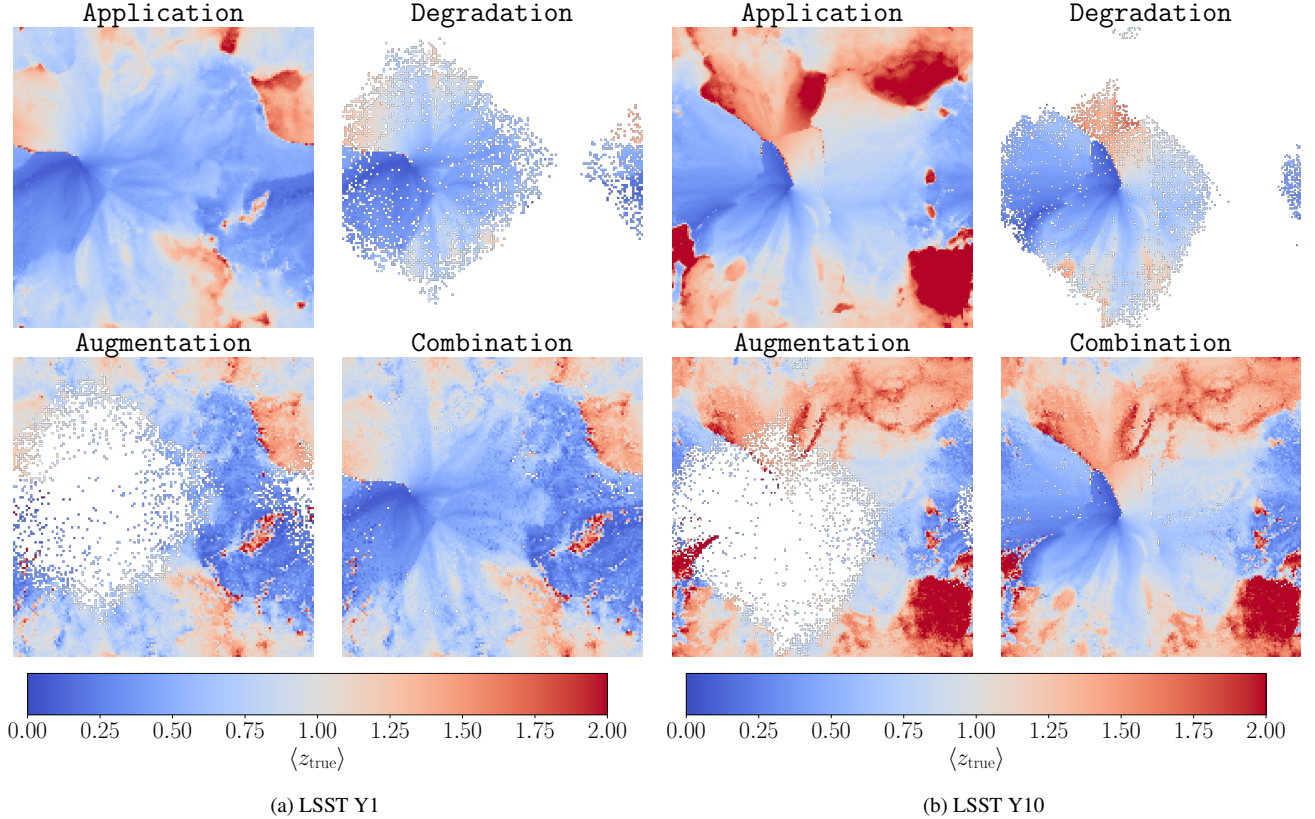
#### 3.1.2 Self-Organising Map

We employ the baseline **Application** dataset to train the SOM algorithm implemented via Somoclu (Wittek et al. 2013) within the RAIL platform. This training compresses the high-dimensional space of a suite of representative galaxy broadband SEDs into a discrete two-dimensional map, with each cell corresponding to a sub-volume of the SED space. We choose the  $i$ -band as the reference, combining its apparent magnitudes with the colours derived relative to it. The SOM grid is configured as  $140 \times 140$  for Y1 and  $180 \times 180$  for Y10, ensuring adequate resolution for accurate mapping between galaxy broadband SEDs and redshifts. A Gaussian kernel with a standard deviation coefficient of 0.5 and a toroidal topology with hexagonal neurons are adopted for the training. The training is initialised using Principal Component Analysis (PCA) and then iterated for 50 epochs with linear cooling of both the neighbourhood radius and learning rate. The pre-trained SOM is subsequently applied to the remaining 500 statistical **Application** datasets, computing the Best Matching Unit (BMU) for each galaxy. To minimise computational costs, we refrain from retraining for each iteration and verify that the random photometric error realisation does not substantially affect the SOM mapping.

In each panel of Figures 3–6, the left panel corresponds to the Y1 scenario and the right to Y10, both illustrating the baseline experi-

**Table 1.** Statistical properties of the baseline *Application* dataset.

Scenario	Number of galaxies	Number density	Effective number density <sup>a</sup>	Limiting magnitude <sup>b</sup>	Gold magnitude <sup>c</sup>
LSST-Y1	2924005	14.77 arcmin <sup>-2</sup>	11.14 arcmin <sup>-2</sup>	25.26	24.05
LSST-Y10	7223012	36.48 arcmin <sup>-2</sup>	27.95 arcmin <sup>-2</sup>	26.51	25.30

<sup>a</sup> Effective number density is defined in [Chang et al. \(2013\)](#).<sup>b</sup>  $i$ -band  $5\sigma$  point-source limiting magnitude under the prescribed observing conditions.<sup>c</sup> Gold magnitude: the  $i$ -band magnitude threshold used for Gold selection, as specified by LSST DESC SRD.**Figure 3.** Colour maps showing the average true redshift per cell for various datasets are presented for Y1 (left panels) and Y10 (right panels), for the baseline experiment. In each panel, the SOM maps for the *Application*, *Degradation*, *Augmentation*, and *Combination* datasets are arranged in the upper left, upper right, lower left, and lower right quadrants, respectively.

ment as a representative example of the full set of 501 realisations. In Figure 3, the upper-left subplot shows the SOM map of mean true redshifts derived from the baseline *Application* dataset. Figures 4 displays the  $u-g$  versus  $g-r$  and  $i-z$  versus  $z-y$  colour-colour diagrams, again with the baseline *Application* data in the upper-left quadrants of each panel. Figure 5 illustrates the distribution of  $g-z$  colour against the  $i$ -band magnitude, whereas Figure 6 shows the galaxy distributions in relation to the true redshifts  $z_{\text{true}}$ . Note that the Y10 dataset contains a higher fraction of galaxies at  $z_{\text{true}} \gtrsim 1.0$  and fainter magnitudes ( $i > 23$ ) than Y1, reflecting its deeper survey depth.

### 3.2 Degradation datasets

After constructing the *Application* datasets, we utilise a two-stage approach to replicate the selection effects arising from compiling multiple spectroscopic surveys. In the initial stage, we impose cuts in magnitude, redshift and colour, and incorporate probabilistic sam-

pling based on spectroscopic success rates. Consequently, we generate 501 unique realisations of spectroscopic datasets that replicate a range of specific spectroscopic surveys. This framework is capable of easily accommodating a diverse range of prospective spectroscopic programmes without being confined to a single survey strategy.

In the second stage, we randomly sample and collect subsets of these realisations to produce 501 *Degradation* datasets, thereby emulating the combination of multiple spectroscopic catalogues into a more representative training dataset for photometric redshift modelling. The *Degradation* datasets therefore collectively capture realistic variations in spectroscopic depth, colour-dependent selection biases and redshift distributions, each of which is forward-modelled as a source of systematic uncertainty in subsequent photometric redshift estimation.

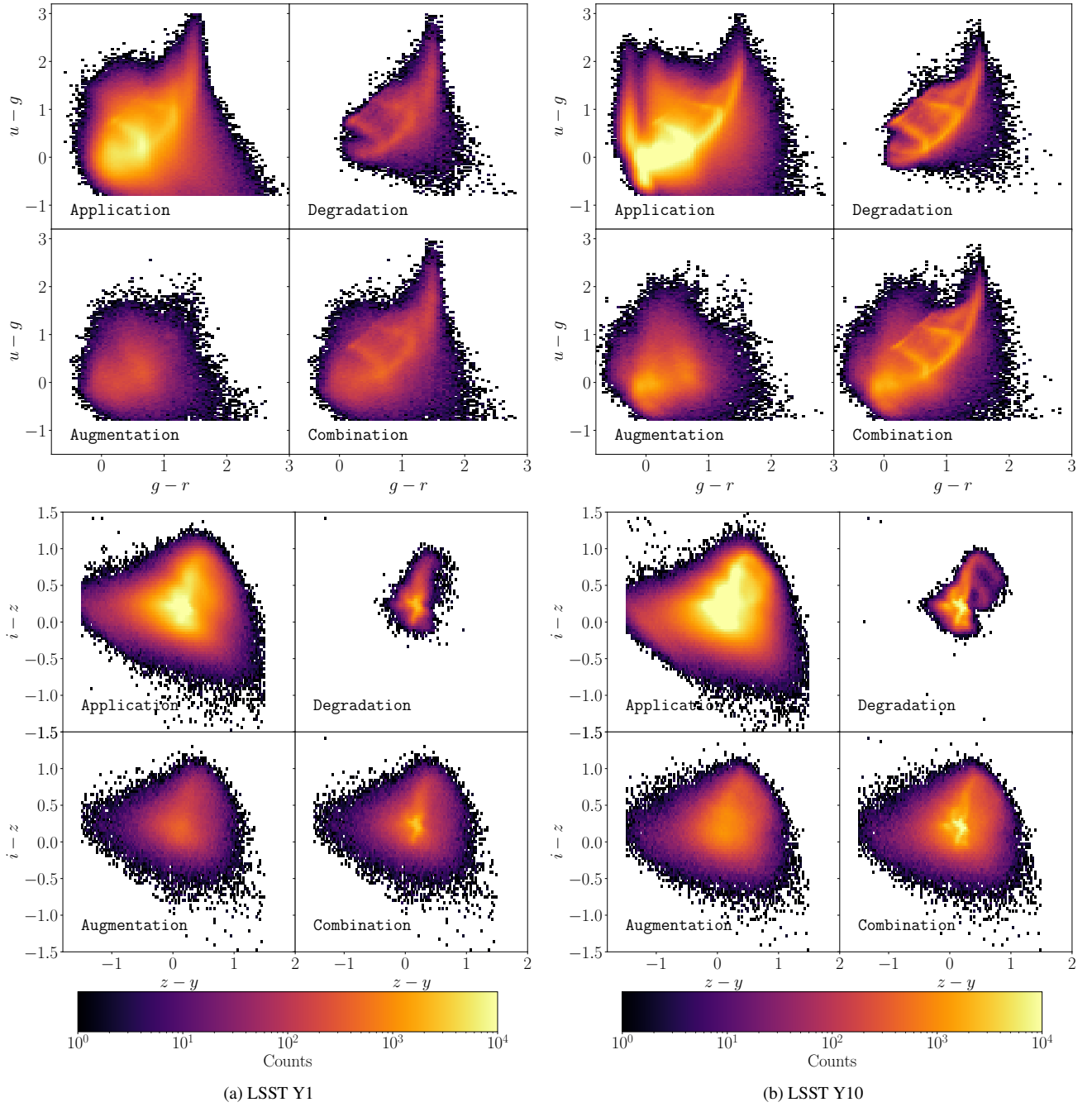


**Figure 4.** Colour–colour diagrams for the baseline experiment, shown for LSST Y1 (left) and Y10 (right). The upper row displays  $u - g$  versus  $g - r$ , while the lower row shows  $i - z$  versus  $z - y$ . Each panel is subdivided into four quadrants, corresponding to the Application (top left), Degradation (top right), Augmentation (bottom left) and Combination (bottom right) datasets.

### 3.2.1 Spectroscopic selection

For each realisation of the Application datasets, we draw an upper limit on the observed  $i$ -band magnitude,  $i_*$ , uniformly from  $20 < i_* < 24$  for Y1 and  $20 < i_* < 25$  for Y10. These intervals mirror the depths of spectroscopic surveys likely to accompany LSST in its early and later operations. Likewise, we assign an upper redshift cut,  $z_*$ , by sampling uniformly within  $0.5 < z_* < 2.5$  for Y1 and  $0.5 < z_* < 3.0$  for Y10.

This parameter configuration anticipates the increasing focus on faint and high-redshift galaxies in upcoming spectroscopic pro-

grammes. These encompass the accumulation of spectroscopy of galaxies through ongoing initiatives, as well as space-based missions like the James Webb Space Telescope (JWST<sup>19</sup>; Gardner et al. 2006), next-generation ground-based facilities – such as the Extremely Large Telescope (ELT<sup>20</sup>; Padovani & Cirasuolo 2023) and Giant Magellan Telescope (GMT<sup>21</sup>; Burgett et al. 2024) – as well as preliminary

<sup>19</sup> <https://webbtelescope.org/home>

<sup>20</sup> <https://elt.eso.org>

<sup>21</sup> <https://giantmagellan.org>



Stage-V spectroscopic surveys, including DESI-II (Schlegel et al. 2022a), the MUltiplexed Survey Telescope (MUST<sup>22</sup>) (Zhao et al. 2024), and other potential candidates (Schlegel et al. 2022b; Besuner et al. 2025).

Furthermore, deep-field spectroscopic programs frequently focus on optically red galaxies due to their robust redshift determination obtained from distinct spectral features, together with their more predictable selection functions, stronger large-scale clustering, and their detectability at greater depths. To simulate this preference, a magnitude-dependent cut in the  $g-z$  colour is applied, characterised by a linear relation with the  $i$ -band magnitude:

$$i - i_* < \tan \varphi_* [(g - z) - (g - z)_*]. \quad (1)$$

Here,  $i_*$  denotes the previously defined upper limit in the  $i$ -band,  $(g - z)_*$  the colour intercept and  $\varphi_*$  the slope angle. For both the LSST Y1 and Y10 scenarios,  $(g - z)_*$  is drawn uniformly from  $[0.5, 2.5]$  and  $\varphi_*$  from  $[0, \pi/2]$ . This criterion approximates the colour-based inclusion and exclusion strategies adopted by deep-field spectroscopic surveys.

In contrast, wide-field campaigns like *Euclid* and DESI also target bluer star-forming galaxies that exhibit prominent emission lines, particularly at high redshift. This selection is mainly influenced by detectability criteria regarding emission line flux and redshift window instead of colour (Cagliari et al. 2024; Raichoor et al. 2023), making them less affected by a red-galaxy exclusion. In order to simulate the influence of more intricate selection functions within the multi-dimensional colour space, we randomly choose SOM cells at a rate  $r_*$ , which is uniformly distributed across the interval  $r \in [0.2, 0.8]$ . This is applied to both the LSST Y1 and Y10 scenarios, with galaxies in the unselected cells being disregarded. Although our probabilistic prior within this parametrised framework is deliberately simplistic, it provides useful flexibility to capture variations in colour thresholds across different surveys. More sophisticated, survey-specific colour boundaries could be incorporated in future developments.

Moreover, we account for the impact of the spectroscopic success rate  $\lambda(i)$  by modelling it as a logistic function of the galaxy  $i$ -band apparent magnitude:

$$\lambda(i) = \frac{1}{1 + \lambda_* \exp [i - i_*]}. \quad (2)$$

In this context,  $i_*$  represents the upper threshold previously defined in the  $i$ -band magnitude for each Application dataset. To introduce additional stochasticity, we draw the parameter  $\lambda_*$  uniformly from the range  $0.5 < \lambda_* < 5.0$  for both Y1 and Y10 scenarios, thereby capturing different levels of spectroscopic survey completeness. This prescription yields an almost complete success rate for the brightest sources ( $i \lesssim 18$ ), followed by a steep decline as the SNR decreases.

Each realisation of the first-stage spectroscopic dataset is obtained by sampling according to Equation 2, yielding  $1.0 \times 10^5$  to  $2.0 \times 10^5$  galaxies for Y1 and  $2.5 \times 10^5$  to  $5.0 \times 10^5$  galaxies for Y10, in line with the expected expansion of spectroscopic coverage. These sample sizes are motivated by deep-field spectroscopic surveys, which cover relatively small areas of sky. By contrast, wide-field campaigns observe orders of magnitude more galaxies; including them in full would cause the spectroscopic training sample to be dominated by their shallower selection functions, introducing a pronounced imbalance between bright and faint galaxies in photometric-redshift training. Consequently, we select a subset of the wide-field spectroscopic datasets of comparable size to our deep-field samples, as reflected in

our configuration. Moreover, given finite computational resources, much larger spectroscopic samples would substantially increase the cost of photometric-redshift training across multiple realisations.

### 3.2.2 Compilation of multiple datasets

Finally, every Degradation dataset is constructed by merging  $M$  randomly chosen realisations, where  $M$  is drawn from  $[4, 6]$  for Y1 and  $[8, 12]$  for Y10, and then downsampling to the same total galaxy counts as the corresponding experiment of spectroscopically-selected galaxies, thereby minimising computational overhead. This procedure produces Degradation datasets that encapsulate multiple realistic spectroscopic selection functions while preserving sufficient variation across experiments.

The Degradation datasets for pre-trained SOM cells are shown in the upper right subplots of each panel in Figure 3, illustrating how spectroscopic selection sculpts the galaxy distribution in SOM space. Notably, many cells, particularly those at higher redshift, become empty due to these selection effects. This sparsity is also evident in the colour-colour diagrams (upper right quadrants of each panel in Figure 4), in the magnitude and colour cuts depicted in Figure 5, and in the lack of galaxies with  $z_{\text{true}} \gtrsim 1.5$  (dark-blue solid lines) in Figure 6. If left uncorrected, such incomplete sampling can heavily bias subsequent photometric-redshift estimates.

## 3.3 Augmentation datasets

To address selection effects introduced by the degradation process, we adopt and extend an augmentation strategy originally proposed by Moskowitz et al. (2024), adapting it for use with a SOM. Our method comprises a dual-phase procedure to construct the Augmentation datasets. Initially, galaxies are sampled from the CosmoDC2 catalogues to ensure their distribution in SOM space corresponds with that of the Application datasets, thus aligning their overall distributions within the multi-dimensional colour-magnitude space. In the second phase, we perform targeted augmentation to populate SOM cells that are under-represented or entirely unoccupied in the corresponding Degradation datasets.

### 3.3.1 Weighted sampling

Initially, CosmoDC2 galaxies are processed using the same pipeline as for the Application datasets. This includes applying LSST photometric errors, perturbing apparent magnitudes, enforcing the LSST DESC SRD Gold selection, and randomly sampling over HEALPix sky pixels to account for spatial variations, under both Y1 and Y10 observing conditions.

Then, the pre-trained SOM is used to map each selected CosmoDC2 galaxy to its BMU in SOM space. We calculate cell-wise occupancy for both the Application datasets and the selected CosmoDC2 galaxies. We then assign sampling weights to the CosmoDC2 galaxies given by the ratio of cell occupancies, ensuring that the synthetic samples reproduce the structure of the Application datasets in SOM space. This selection and re-weighting procedure is repeated over 501 independent experiments, one baseline and 500 statistical runs, each matched in size to their respective Application datasets to minimise excessive manipulation.

<sup>22</sup> <https://must.astro.tsinghua.edu.cn>

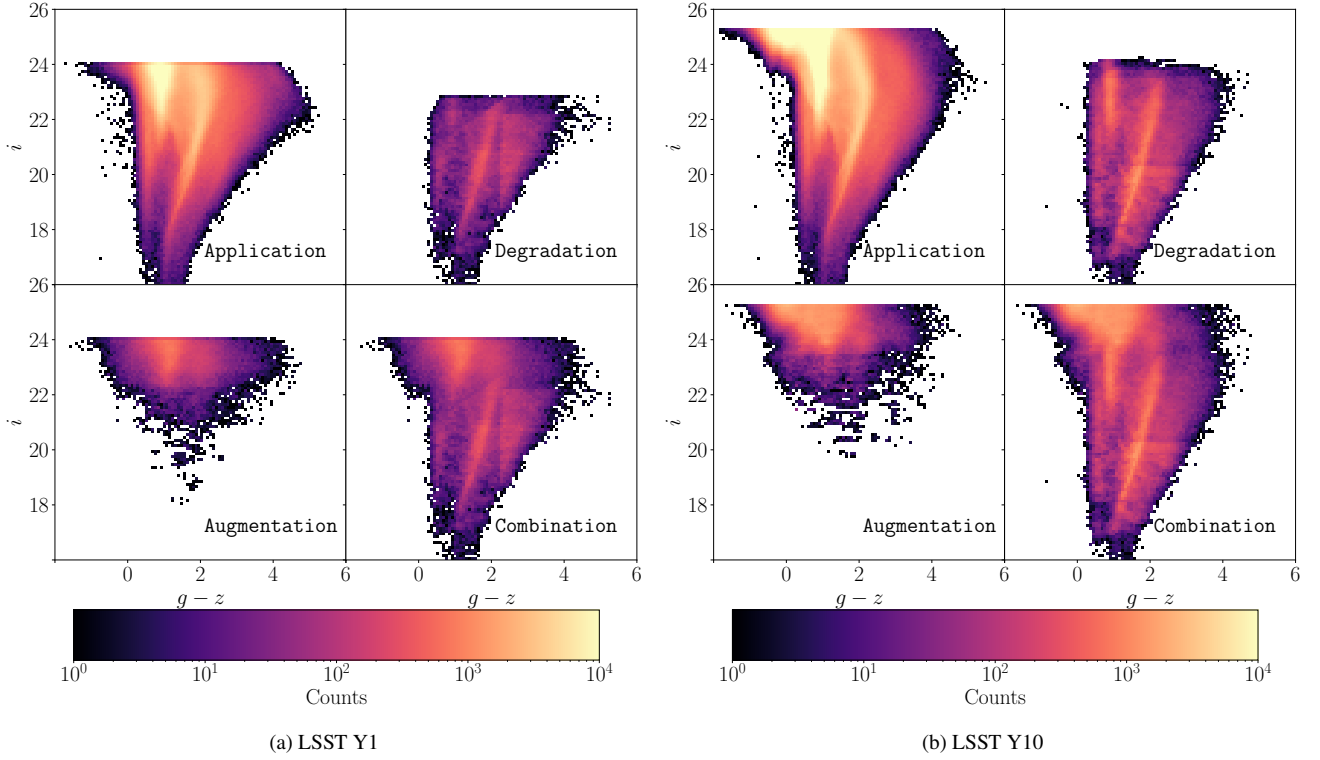


**Figure 5.**  $g - z$  colours versus  $i$ -band apparent magnitudes for various datasets are displayed for Y1 (left panel) and Y10 (right panel), under the baseline experiment. In each panel, the upper left, upper right, lower left, and lower right quadrants correspond to the Application, Degradation, Augmentation, and Combination datasets, respectively.

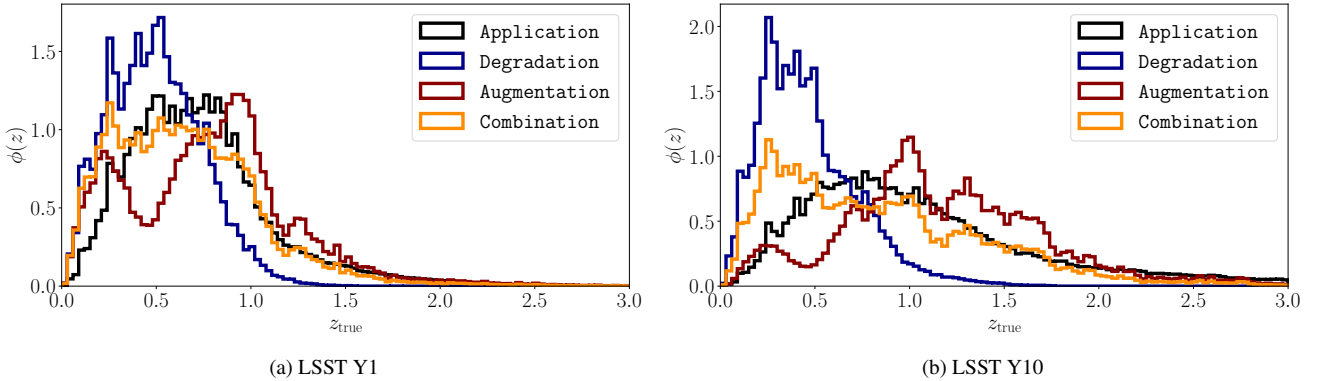


**Figure 6.** Normalised ensemble distributions of galaxy true redshifts for various datasets are displayed for Y1 (left panel) and Y10 (right panel), under the baseline experiment. In each panel, the black, dark-blue, dark-red, dark-orange correspond to the Application, Degradation, Augmentation, and Combination datasets, respectively.

### 3.3.2 Adaptive data augmentation

To mitigate incomplete sampling within the SOM space of the Degradation datasets, we build upon the matched CosmoDC2 galaxies. First, we identify SOM cells unoccupied in the Degradation datasets and repopulate them using corresponding galaxies from the matched CosmoDC2 pool. Moreover, we identify galaxies that surpass the maximum redshift and magnitude limits of the Degradation datasets, integrating them into the Augmentation datasets as well, to ensure that previously excluded populations are considered.

To adaptively regulate the number of augmented galaxies, we compute  $f_*$ , defined as the fraction of Application galaxies that fall into SOM cells absent from the Degradation dataset. We then set the

target Augmentation-to-Degradation ratio to  $f_* (1 + f_*)$ , thereby smoothly scaling the size of the augmented sample to balance the two datasets. In the limit of minimal spectroscopic incompleteness  $f_* \ll 1$ , this prescription closely approximates the ideal augmentation ratio  $\frac{f_*}{1 - f_*}$ . Conversely, under the most extreme degradation scenarios where  $f_* \rightarrow 1$ , this ratio is restricted to a maximum of 2. This effectively caps the augmentation, thereby preventing the photometric-redshift training from being excessively influenced by synthetic galaxies.

The distribution of galaxies within the Augmentation datasets is also projected onto pre-trained SOM cells, as depicted in the lower left subplots of each panel in Figure 3–5, demonstrating how data

augmentation compensates for missing information within the SOM space, colour-colour diagrams, colour-magnitude diagram, respectively. Further evidence of the effectiveness of augmentation is visible in the increased presence of galaxies at  $z_{\text{true}} \gtrsim 1.5$  (highlighted in dark-red solid lines) in Figure 6.

As shown in Figure 1, the colour distributions of CosmoDC2 and OpenUniverse2024 differ markedly in  $u-g$  and  $g-r$ . In contrast, Figures 4 reveals that the Augmentation datasets exhibit substantially improved agreement with the Application datasets, owing to SOM-based weighted resampling. By matching CosmoDC2 galaxies to occupied SOM cells, we correct misalignments introduced by the distinct SED models, particularly at the bright, low-redshift end where the two catalogues overlap.

For faint, high-redshift galaxies, the differences between the SED models become more pronounced, leading to non-overlapping colour distributions, as previously shown in Figure 1. Consequently, certain galaxy populations in the Application datasets remain unrepresented in the Augmentation datasets despite weighted resampling. For example, in the LSST Y10 scenario of Figure 4, an elongated locus of galaxies with  $g-r \approx -0.5$  and  $0.0 \lesssim u-g \lesssim 3.0$  is present in the Application dataset but absent in the Augmentation dataset. Such persistent gaps can bias inferred galaxy properties and introduce systematic errors into subsequent analyses.

### 3.4 Combination datasets

By merging the Degradation and Augmentation datasets, the resulting Combination datasets offer enhanced representativeness of galaxy broadband SEDs compared to the photometric Application datasets, as opposed to the unaugmented Degradation datasets. The lower right subplots in each panel of Figure 3 display the mean true redshifts of SOM cells occupied by the Combination datasets, demonstrating significantly enhanced coverage of the SOM cells compared to the Degradation datasets alone.

Similarly, in the colour-colour and colour-magnitude diagrams presented in the lower right subplots of each panel in Figure 4–5, combining the sparse Degradation datasets, which have notable deficits at fainter magnitudes and specific colour regimes, with the targeted Augmentation datasets results in Combination datasets that more effectively span the parameter space. The resultant distributions closely resemble the overall Application datasets, reducing incompleteness.

Figure 6 further demonstrates these gains. The under-densities at intermediate redshifts evident in the Degradation samples are filled by the extended tails of the Augmentation distributions, yielding a well-balanced redshift histogram in the Combination datasets. Here, the augmented datasets (dark-orange solid lines) more faithfully reproduce the full Application redshift distributions (black solid lines).

Compared to the original implementation of data augmentation in Moskowitz et al. (2024), which employed simplified assumptions regarding the boundaries of  $g-z$  colour,  $i$ -band magnitude and redshift, our SOM-based approach can accommodate far more complex selection functions in the multi-dimensional colour–magnitude space.

Figure 4 demonstrates the robustness of our SOM-based augmentation in colour–colour diagrams, where no regular boundary geometry is discernible. By visualising the multi-dimensional colour–magnitude space via the SOM, we can readily identify sparsely sampled regions and apply targeted data augmentation.

Similarly, as illustrated in the left panel of Figure 5, the

colour–magnitude boundary of the Degradation dataset no longer conforms to a simple linear relation, owing to the amalgamation of multiple mock spectroscopic surveys. Nonetheless, our SOM-based augmentation adaptively compensates for gaps in spectroscopic coverage, rendering it well suited to future analyses involving complex selection functions.

However, this compensation is not entirely flawless: a noticeable deficit of galaxies around the boundaries remains. This phenomenon arises from our current definition of the Augmentation dataset, which augments only wholly empty SOM cells, whereas sparsely occupied cells may also require supplementary galaxies. For truly optimal performance, a comprehensive investigation of the ideal threshold for SOM cell occupancy – potentially with adaptive thresholds for each Degradation dataset – is necessary, and constitutes an avenue for future study.

Furthermore, some SOM cells remain unpopulated or sparsely occupied even after augmentation, reflecting persistent SED model discrepancies between CosmoDC2 and OpenUniverse2024. These gaps manifest most clearly as an underestimation of the high-redshift tail ( $z_{\text{true}} \gtrsim 2.0$ ), particularly in the Y10 scenario, indicating amplified mismatches for faint, distant galaxies. Moreover, variability in the spectroscopic selection functions applied during degradation translates into differing augmentation requirements across realisations, introducing an additional systematic uncertainty that we exploit to assess the impact of incomplete coverage and selection-induced biases on photometric-redshift estimation.

## 4 PHOTOMETRIC REDSHIFT ESTIMATION

Thanks to data augmentation, the spectroscopically informed datasets are highly representative and ideally suited for estimating photometric redshifts using machine learning, thus negating the need for predefined galaxy SED templates. However, future research into template-driven and hybrid methods would be valuable, despite being outside the scope of this study.

In this section, we first introduce the FlexZBoost photometric redshift estimation method, and describe the definitions different galaxy sub-samples based on the point estimates of photometric redshifts. Although we use this specification here to characterise our photometric-redshift quality, the SOM-based augmentation method and the resulting datasets are applicable to many other science cases.

### 4.1 Machine learning modelling

Based on a detailed comparative analysis with established methods (Schmidt et al. 2020), FlexZBoost (Izbicki & Lee 2017; Dalmasso et al. 2020) has demonstrated superior performance in estimating both the conditional probability density function (PDF) of photometric redshifts and the corresponding point estimates from galaxy colours. We therefore employ FlexZBoost in our proof-of-concept study to validate the efficacy of our SOM-based data augmentation, deferring evaluation of alternative photometric-redshift estimators to future work.

FlexZBoost is built on the Flexcode framework, which models the conditional density  $p(z | \mathcal{T})$  for a given galaxy training dataset  $\mathcal{T}$  by projecting it onto an orthogonal basis of functions  $O_k(z)$   $p(z | \mathcal{T}) \equiv \sum_k q_k(\mathcal{T}) O_k(z)$ . Broadband photometry is therefore used to infer the expansion coefficients  $q_k(\mathcal{T}) = \int p(z | \mathcal{T}) O_k(z) dz = \langle O_k(z) | \mathcal{T} \rangle$ , which represent the conditional expectations of the basis functions. By employing regression in a high-



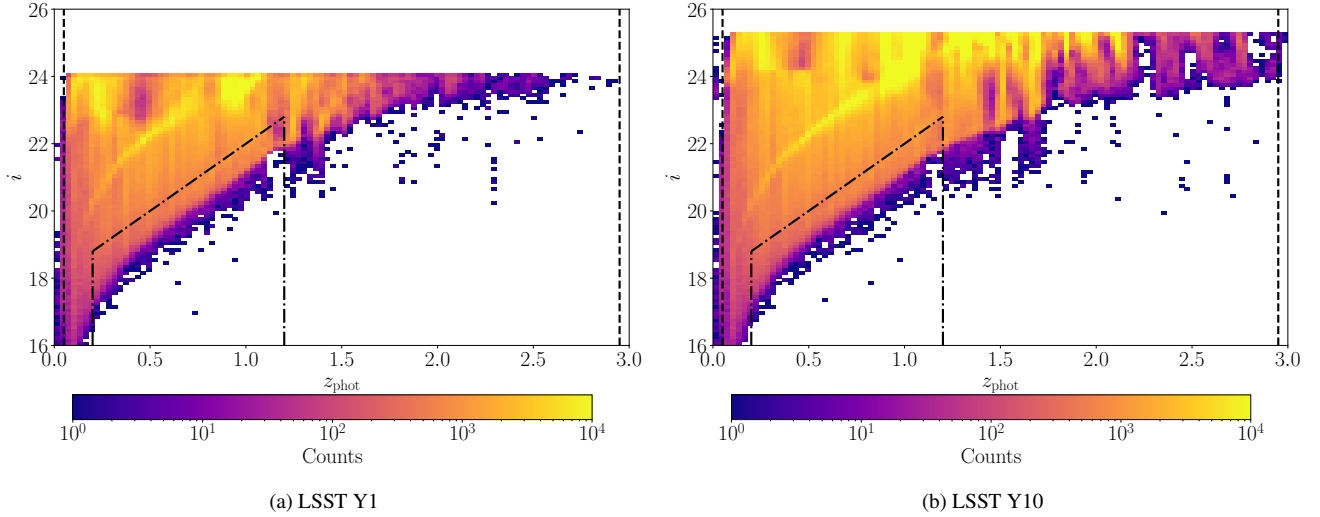


**Figure 7.** Colour maps depicting the galaxy distribution, with the  $i$ -band magnitude on the y-axis and photometric redshift estimates,  $z_{\text{phot}}$ , on the x-axis, for LSST Y1 (left) and Y10 (right) under the baseline experiment. Black dashed lines indicate the selection range  $0.05 \leq z_{\text{phot}} \leq 2.95$  used to identify source galaxies, while black dot-dashed lines represent the redshift-dependent magnitude limits imposed on lens galaxies (Porredon et al. 2021).

dimensional feature space, FlexZBoost effectively captures complex, non-linear mappings between galaxy colours and redshift.

Utilising the FlexZBoost implementation available on the RAIL platform, we develop our photometric redshift model using the Combination dataset, which integrates "observed" spectroscopic-like Degradation data with "simulated" Augmentation samples. This dataset is divided into training and validation sets in an 80%:20% proportion to perform regression on the hyperparameters of FlexZBoost, including the bump optimisation and sharpness parameters. The  $i$ -band apparent magnitude serves as the reference baseline against which all multi-band colours are defined.

We approximate the conditional PDF using a Fourier basis of up to 50 orthogonal functions uniformly covering  $0.0 \leq z \leq 3.0$  in steps of 0.01. Bump optimisation parameters are sampled over  $[0.0, 0.5]$  on a 50-point grid, and sharpness parameters over  $[0.5, 2.5]$  with the same grid resolution. For regression, we employ XGBoost (Chen & Guestrin 2016), minimising the Mean Squared Error (MSE) with a maximum tree depth of 8 and a learning rate of 0.1 – choices that balance model expressivity with computational efficiency. Following hyperparameter tuning, the model is retrained on the complete Combination dataset. This rigorous framework provides both flexibility and robustness, effectively capturing the intrinsic complexity of galaxy populations while mitigating the risk of overfitting.

After training the FlexZBoost models using 501 experiments from the Combination dataset, each optimised model is applied to its respective experiment within the photometric Application datasets. This process generates the conditional density  $p(z|S_n, \mathcal{P}_n)$  for each galaxy, with  $S_n$  and  $\mathcal{P}_n$  representing the spectroscopic Combination and photometric Application datasets, respectively, for the  $n$ th experiment. These conditions take into account variations in photometric noise, spatial coverage, and spectroscopic selection functions. We smoothly interpolate the conditional density over the interval  $[0.0, 3.0]$  with redshift increments of 0.01, determining the point estimates  $z_{\text{phot}}$  as the redshift that maximises the conditional PDF for each galaxy.

## 4.2 Definition of source and lens samples

Based on point estimates, we first identify galaxies therefore serving as the background source galaxies that are gravitationally lensed by intervening mass distributions in the Universe (Asgari et al. 2021; Amon et al. 2022; Secco et al. 2022; Li et al. 2023c; Dalal et al. 2023; Li et al. 2023a; Dark Energy Survey and Kilo-Degree Survey Collaboration et al. 2023; Stölzner et al. 2025; Wright et al. 2025b), therefore targeting galaxies with reliable measurements on weak gravitational lensing signal. Initially, we estimate the shear measurement noise,  $\sigma_\gamma$ , for individual galaxies using the expression provided in (Bernstein & Jarvis 2002), written as

$$\sigma_\gamma = \frac{a}{\mu} \left[ 1 + \left( \frac{b}{\eta} \right)^c \right]. \quad (3)$$

The coefficients in the equation are  $(a, b, c) = (1.58, 5.03, 0.39)$  as defined by Chang et al. (2013). In this calculation, as we described in Section 2, the variable  $\mu$  represents the SNR of coadded  $r$ - and  $i$ -band photometry, while  $\eta$  signifies the squared ratio of the galaxy sizes of galaxies comparing to those of PSFs. Subsequently, we implement a selection criterion of  $\sigma_\gamma < \sigma_\epsilon$ , where  $\sigma_\epsilon$  represents the intrinsic shape noise, presumed to be 0.26.

On top of the constraints on the shear measurement noise  $\sigma_\gamma$ , we further restrict our sample to galaxies with photometric redshifts in the range  $0.05 < z_{\text{phot}} < 2.95$ . This excludes objects at the boundaries of the redshift PDF, where asymmetries can lead to significant errors, and minimises contamination from higher-redshift ( $z > 3.0$ ) galaxies, which contribute little to the lensing signal but complicate redshift calibration in a real analysis.

Additionally, we define another foreground galaxy subset, referred to as lens samples, selected via precise redshift estimations to trace high-mass haloes for large-scale structure studies (Heymans et al. 2021; Abbott et al. 2022; Dvornik et al. 2023; Sugiyama et al. 2023; Miyatake et al. 2023). We adopt the redshift-dependent magnitude cut of Porredon et al. (2021),  $i < 4 \cdot z_{\text{phot}} + 18$ , valid for  $0.2 < z_{\text{phot}} < 1.2$ . For both LSST Y1 and Y10, we apply the same criterion in accordance with the stringent photo- $z$  precision requirements of the LSST DESC SRD. Future work should explore the inclusion of fainter galaxies in the Y10 lens samples – while increased number density

may enhance statistical power, it could also degrade redshift accuracy – necessitating further investigation to optimise selection strategies (Moskowitz et al. 2023).

Figure 7 shows the distribution of galaxies in  $i$ -band magnitude versus photometric redshift  $z_{\text{phot}}$ . Black dashed lines denote the source sample selection boundaries, which remove objects near analysis limits to prevent bias in the conditional density estimates, while black dot-dashed lines indicate the lens sample selection, isolating brighter galaxies to secure high photo- $z$  precision. The distribution becomes increasingly disordered at faint magnitudes, highlighting the challenge of moving from training on Degradation datasets derived from OpenUniverse2024 to using Augmentation datasets drawn from CosmoDC2. In the Y1 case, the spectroscopic selection limit, especially for  $20 \lesssim i_* \lesssim 22$ , noticeably biases redshift estimates at  $z_{\text{phot}} \gtrsim 1.0$ . By contrast, the deeper spectroscopic coverage in Y10 mitigates this bias, underscoring the importance of consistent lens sample definitions across survey epochs.

## 5 RESULTS AND DISCUSSION

In this section, we introduce the statistical metrics used to characterise the precision of our photometric redshifts. We then assess the accuracy of the point estimates and evaluate the performance of the conditional-density modelling, thereby validating our data-augmentation technique via comparative analysis.

### 5.1 Statistical metrics

We quantify the systematic error of each photometric-redshift estimate  $z_{\text{phot}}$  relative to its true redshift  $z_{\text{true}}$  by defining the scaled bias

$$\delta_z = \frac{z_{\text{phot}} - z_{\text{true}}}{1 + z_{\text{true}}}. \quad (4)$$

From the distribution of  $\delta_z$ , we derive two robust metrics for any galaxy subset. First, the median scaled bias,  $\bar{\delta}_z \equiv \text{median}(\delta_z)$ , is adopted in preference over the mean to mitigate sensitivity to outliers. Second, the Normalised Median Absolute Deviation (NMAD) of  $\delta_z$ , denoted  $\sigma_z$ , is defined as

$$\sigma_z = 1.4826 \times \text{median}(|\delta_z - \bar{\delta}_z|). \quad (5)$$

The factor 1.4826 rescales the median absolute deviation into an estimator equivalent to the standard deviation for a Gaussian distribution.

Furthermore, we consider the proportion at which galaxies fall outside the outlier boundary  $|\delta_z| = 0.15$ , as defined in previous studies (e.g. Fotopoulou et al. 2012; Yang et al. 2014; Davidzon et al. 2017; Brinchmann et al. 2017; Duncan et al. 2019), termed outlier fraction,

$$f_o = \frac{N_g(|\delta_z| > 0.15)}{N_g}, \quad (6)$$

where  $N_g$  represents the total count of a specific galaxy subset. In addition, we incorporate the rates of catastrophic failures where  $|z_{\text{phot}} - z_{\text{true}}| > 1.0$ , as outlined in Moskowitz et al. (2024), denoted as

$$r_c = \frac{N_g(|z_{\text{phot}} - z_{\text{true}}| > 1.0)}{N_g}. \quad (7)$$

These metrics evaluate the prevalence of notable systematic errors

in the photometric-redshift determinations. In addition to point estimates, we evaluate the performance of the photometric-redshift conditional density modelling,  $p(z|\mathcal{S}_n, \mathcal{P}_n)$ . For simplicity, the explicit dependence on the  $n$ th spectroscopic dataset  $\mathcal{S}_n$  and photometric dataset  $\mathcal{P}_n$  will henceforth be omitted. We employ the cumulative distribution function,

$$q(z) \equiv \int_0^z p(z') dz', \quad (8)$$

to define summary statistics owing to its well-behaved, bounded range. The Probability-Integral-Transform (PIT) value – defined as the CDF evaluated at the true redshift  $z_{\text{true}}$ ,  $q(z_{\text{true}})$  – has been widely used in the literature (e.g. Bordoloi et al. 2012; Freeman et al. 2017; Tanaka et al. 2018; Schmidt et al. 2020). For an ideal conditional density model, the PIT values for any galaxy subset should follow a uniform distribution; deviations from uniformity therefore quantify information loss during the modelling procedure.

The normalised PIT histograms,  $\mathcal{H}_k[q(z_{\text{true}})]$  for  $k = 1, \dots, K$ , are calculated across  $K = 10$  equally sized quantile bins, ranging from  $[0.0, 1.0]$ , with intervals of 0.1. We calculate these histograms for both the full lens and source samples as well as for each redshift interval defined above. Thus, for each normalised PIT histogram, we then define the divergence loss,  $\mathcal{D}_q$ , as the Root-Mean-Square deviation of the normalised PIT histogram from uniformity:

$$\mathcal{D}_q = \sqrt{\frac{1}{K} \sum_{k=1}^K \{\mathcal{H}_k[q(z_{\text{true}})] - 1\}^2}, \quad (9)$$

where unity denotes the value of the normalised histogram for an ideal uniform distribution. This metric provides a rigorous assessment of the conditional-density modelling quality.

For the lens sample, each metric is assessed across five redshift intervals, each with a width of 0.3, covering the range  $0.0 < z_{\text{true}} < 1.5$ . Similarly, for the source sample, five intervals of equal width are used, encompassing  $0.0 < z_{\text{true}} < 3.0$ . The outcomes of our statistical metrics are depicted as a function of true redshift in Figure 8, with comprehensive discussions provided thereafter.

It is important to note that this interval binning is solely used for assessing the performance of the photometric redshifts, rather than for tomographic binning in cosmological analysis. The latter is based on the derived point estimates and will be addressed in our subsequent paper.

### 5.2 Evaluation of point estimate accuracy

Figure 9 provides a direct visual assessment of the performance of our photometric redshift model under the baseline experiment. As depicted in the top panels of Figure 9, the self-training on the Combination dataset shows excellent agreement between  $z_{\text{phot}}$  and  $z_{\text{true}}$ , indicating that our photometric redshift model reliably captures the colour-redshift relation. By selecting the peak of the conditional PDF, we achieve negligible bias for both the bright lens sample (left panels) and the fainter source sample (right panels), even at  $z_{\text{true}} \gtrsim 1.5$ . The resulting median absolute values of the scaled biases,  $|\bar{\delta}|_z$  consistently meet the LSST DESC SRD requirements for almost the entire redshift range. Hence, with a fully representative spectroscopic training set, FlexZBoost can provide photometric-redshift estimates of outstanding accuracy.

Upon utilising the complete photometric Application datasets, the central panels of Figure 9 demonstrate that the lens galaxies maintain a similar level of performance. In the bottom-left subplots for

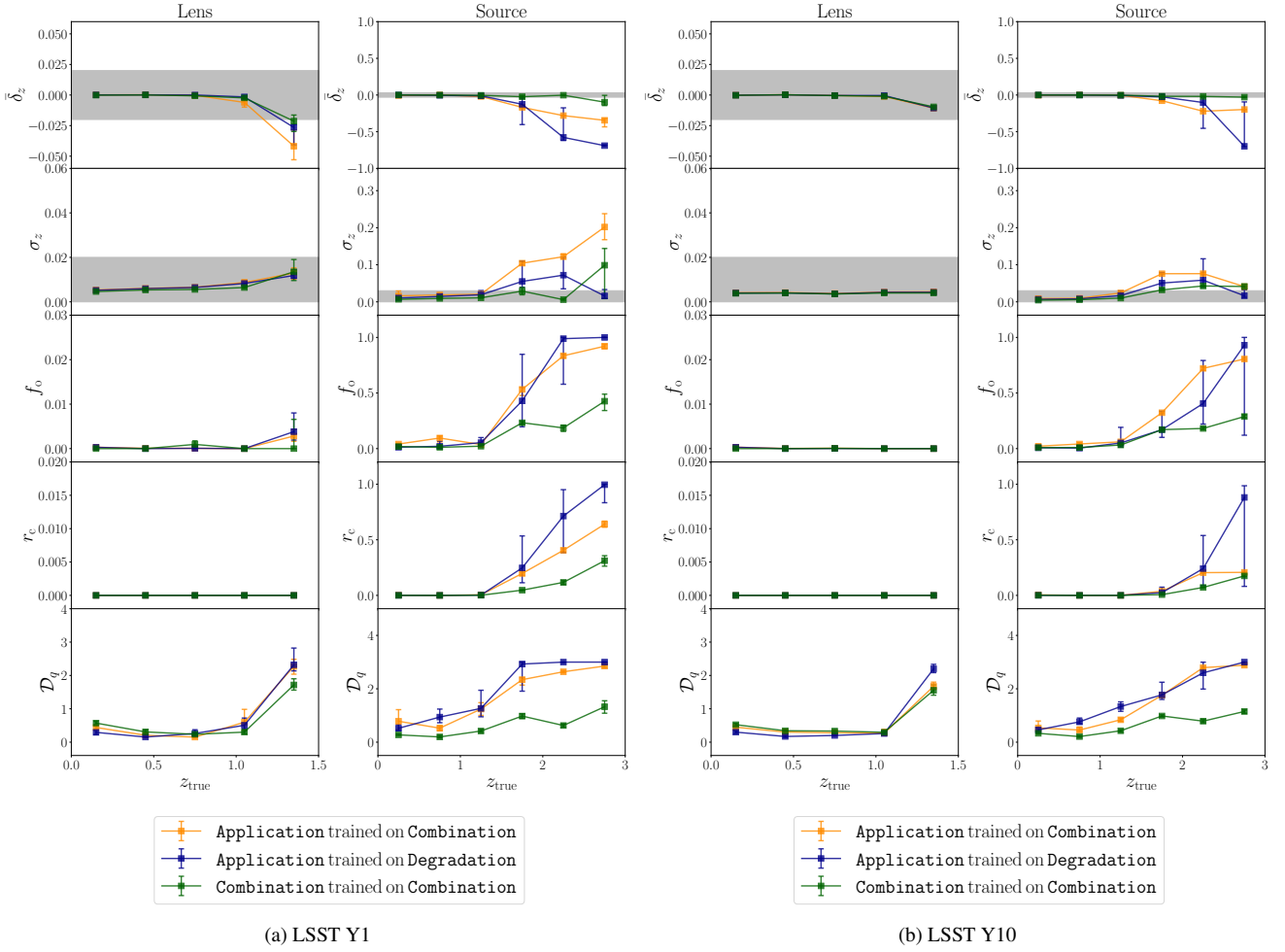


**Figure 8.** Statistical metrics plotted as a function of true redshift, with LSST Y1 in the left panel and LSST Y10 in the right. Within each panel, the metrics are ordered from top to bottom: the median scaled bias  $\bar{\delta}_z$ ; the normalised median absolute deviation (NMAD) of the scaled bias  $\sigma_z$ ; the outlier fraction  $f_o$ ; the catastrophic failure rate  $r_c$ ; and the divergence loss of the normalised PIT histogram  $\mathcal{D}_q$ . In each row, the left and right subplots correspond to the lens and source samples, respectively. Filled markers denote the median value of each metric across all experiments, with error bars indicating the central 68% confidence interval. Green curves show results from self-training on fully representative Combination datasets (ideal benchmarks); orange curves correspond to Application datasets trained on these augmented Combination datasets; and blue curves represent Application datasets trained on the unaugmented Degradation datasets. The grey bands indicate the range defined for LSST DESC SRD.

both the Y1 and Y10 Application lens samples, the median absolute values of the scaled biases,  $|\bar{\delta}|_z$ , highlighted by the black dashed lines, are notably beneath the thresholds set by the LSST DESC SRD, depicted by black dotted lines. This signifies an exceptionally accurate model for this luminous population. Furthermore, practically no outliers or catastrophic failures occur in either instance, reinforcing the robustness of our photometric-redshift point estimates for bright galaxies and thus supporting precision cosmology through large-scale-structure analyses. In contrast, for the source samples,  $|\bar{\delta}|_z$  remains close to the SRD requirement up to  $z_{\text{true}} \lesssim 1.5$ . Nonetheless, a considerable residual bias becomes evident at  $z_{\text{true}} \gtrsim 1.5$ .

Similar trends are evident in Figure 8, where the green and orange curves both correspond to models trained on the Combination datasets but evaluated on the Combination and Application datasets, respectively. This comparison shows that, for the lens sample, both the median scaled bias  $\bar{\delta}_z$  and its NMAD  $\sigma_z$  remain within the grey band defined by the LSST DESC SRD in all cases. For the source sample, however, we observe a significant increase in  $\bar{\delta}_z$ ,

accompanied by a rise in its NMAD, as well as marked increases in the outlier fraction  $f_o$ , and the catastrophic failure rate  $r_c$ .

This suggests that the machine-learning model struggles to extrapolate beyond its training domain in colour–SED space. Contributing factors include photometric noise – which perturbs the mapping between observed SEDs and redshift, particularly for faint galaxies, thereby introducing uncertainty into  $z_{\text{phot}}$  – and systematic mismatches in SED properties. Specifically, the redshift upper limit of the Degradation dataset compels the model to rely on subtly discrepant galaxies in the augmented training dataset – enhanced with high-redshift CosmoDC2 galaxies – compared to those in the photometric Application dataset from OpenUniverse2024. As discussed in Section 3, this SED discrepancy constitutes a primary source of bias in our photometric-redshift modelling.

The bottom two panels of Figure 9 provides a qualitative comparison of photometric-redshift estimates trained exclusively on the Degradation datasets without augmentation. For the lens samples, incorporating the Augmentation datasets yields only marginal improvements: the median absolute scaled biases remain effectively



unchanged whether or not augmentation is applied. Nonetheless, for the source sample in the Y1 scenario, training on the unaugmented **Degradation** dataset results in virtually no galaxies with  $z_{\text{phot}} \gtrsim 1.5$ . A quantitative comparison of the orange and blue curves in Figure 8 reinforces these conclusions. For the lens sample, these curves coincide nearly perfectly across all statistical metrics in both the LSST Y1 and Y10 cases. This reflects that the brightest galaxies are already well represented in the spectroscopic training sets.

Conversely, not employing data augmentation for the source sample results in significantly high outlier fractions ( $f_o \gtrsim 0.5$ ) and catastrophic failure rates ( $r_c \gtrsim 0.5$ ) at  $z_{\text{true}} \gtrsim 2.0$  in the LSST Y1 scenario. Introducing SOM-based data augmentation reduces the outlier fraction by approximately 10–20%, lowers the catastrophic failure rate by a factor of  $\sim 2$ , and decreases the median scaled bias by a factor of  $\sim 2$ –3, thereby demonstrating the efficacy of augmentation in mitigating both bias and outliers in LSST Y1 photometric redshift point estimates. Although the NMAD of the scaled bias  $\sigma_z$  increases after data augmentation, this does not indicate a degradation in photometric performance. On the contrary, the low NMAD observed without augmentation is driven by a high fraction of catastrophic failures, which cluster galaxies around large bias values as seen in Figure 9. Consequently, the rise in NMAD post-augmentation reflects the suppression of these extreme biases. Furthermore, the pronounced strip-like features evident in Figure 9 after augmentation reflect intrinsic degeneracies in galaxy SEDs: in the absence of representative high-redshift training samples, such galaxies would otherwise be classified as catastrophic failures and, consequently, vanish from the regime around one-to-one sequence.

In the LSST Y10 scenario, the **Degradation** datasets comprise deeper spectroscopic observations than in Y1, thereby yielding improved photometric redshift performance for source galaxies even without augmentation. Nonetheless, training with the **Augmentation** datasets still confers benefits: both the median scaled bias  $\bar{\delta}_z$  and the catastrophic failure rate  $r_c$  decrease by up to a factor of two in the highest-redshift interval ( $2.5 < z_{\text{true}} < 3.0$ ). However, in the Y10 case the gains are not uniform across all metrics. For instance, between  $1.5 < z_{\text{true}} < 2.5$ , the outlier fraction  $f_o$  increases, accompanied by modest rises in the median scaled bias and its NMAD. This is likely due to residual mismatches in galaxy SEDs, reflecting limitations of our current augmentation implementation. As shown in Figure 1, the divergence between the CosmoDC2 and OpenUniverse2024 SEDs becomes more pronounced for the fainter galaxies probed at Y10 depths, which can introduce ambiguity into photometric-redshift training and degrade performance. This underscores the necessity for enhancing our augmented mock catalogues in preparation for future LSST Y10 photometric redshift analyses.

Moreover, for both Y1 and Y10 scenarios, the large error bars on the blue curves denote substantial scatter in performance across unaugmented experiments – highlighting sensitivity to the spectroscopic selection function – whereas these variations are significantly reduced in the orange curves once augmentation is applied. Although the augmentation is not flawless, this reduced scatter across all metrics help demonstrate the efficacy of data augmentation.

### 5.3 Assessment of conditional density modelling

In parallel with our point-estimate analysis, we also evaluate the quality of conditional density modelling. In the top panels of Figure 10, the normalised PIT histograms for the **Combination** datasets demonstrate the conditional-density performance under fully representative training. For the lens samples, in both the Y1 and Y10 sce-

narios, a central peak exceeding unity is observed, along with dips falling below the flat line near  $q(z_{\text{true}}) = 0$  and 1, across all subsets at varying redshifts. This indicates that the conditional-PDF widths for these bright populations are slightly overestimated, resulting in an excess of objects at intermediate quantiles. Such over-smoothing stems from the basis-function decomposition of the density model, since photometric redshift estimates for the low-redshift brightest galaxies would otherwise be expected to be sharply constrained.

The normalised PIT histogram of the all source galaxies, as shown in the solid black curve, reveal elevated values at the quantile boundaries, whilst the central peak approximates unity. Comparable patterns can be observed in histograms of low-redshift sources ( $z_{\text{true}} \lesssim 1.5$ ), which suggests their predominance in the overall distribution. This pattern indicates that the conditional-PDF of faint, low-redshift galaxies – whose SEDs could be confused with those of higher-redshift objects – are either underestimated regarding widths or systematically biased, unlike the bright lens samples. In the high-redshift region ( $z_{\text{true}} \gtrsim 1.5$ ), the histogram presents a marked slope even with fully representative training, suggesting a continuing systematic bias. These trends are also demonstrated in the increasing divergence loss of normalised PIT histograms in the bottom row of Figure 8, which correspond to the rise in point-estimate outliers and catastrophic failures, highlighting the difficulty of modelling precise PDFs at high redshifts.

In the central panels of Figure 10, consistent with our point-estimate results, applying the photometric-redshift model to the **Application** datasets leaves the lens-sample PIT distributions largely unchanged but precipitates a pronounced deterioration in the source-sample performance. In particular, at  $z \gtrsim 1.5$ , the slope of the PIT histogram becomes markedly steeper, indicating a significant increase in average bias for faint galaxies. This trend is also reflected in the upward shift of the divergence-loss curves from green (**Combination** datasets) to orange (**Application** datasets) in Figure 8. These findings emphasise that the inclusion of faint, high-redshift galaxies – coupled with photometric noise and non-representative SEDs in the training data – exacerbates the challenges of conditional-density modelling, especially for high redshift galaxies. This is one of the primary challenges in calibrating ensemble redshift distributions and will be addressed in detail in our forthcoming paper, where we will explore how various estimators can be combined to mitigate systematic biases at the population-level.

Comparison with models trained solely on the unaugmented **Degradation** dataset further emphasises the benefits of data augmentation for conditional-density modelling. For the lens sample, augmentation induces a negligible change. In contrast, for the source sample under the LSST Y1 scenario, the divergence loss of the normalised PIT histogram decreases by approximately 25–50% even at low redshift ( $z_{\text{true}} \lesssim 1.5$ ), whereas improvements in point-estimate metrics remain largely confined to high-redshift galaxies. This effect is evident in the lower panels of Figure 10. With augmented training, the edge peaks of the normalised PIT histograms in the low-redshift bins are moderately suppressed and the central values approach unity, yielding distributions that are closer to uniform. This improvement arises from a more faithful representation of SED degeneracies, owing to the inclusion of high-redshift galaxies in the photometric-redshift training.

At high redshift ( $z_{\text{true}} \gtrsim 1.5$ ) in the LSST Y1 scenario, the unaugmented PIT histograms collapse to near zero except for a spike at  $q(z_{\text{true}}) = 1$ , indicative of pronounced systematic biases, consistent with the trends in Figures 8 and 9. Training on the augmented **Combination** datasets still produces a tilt relative to a uniform distribution, but a substantial fraction of galaxies exhibit markedly reduced

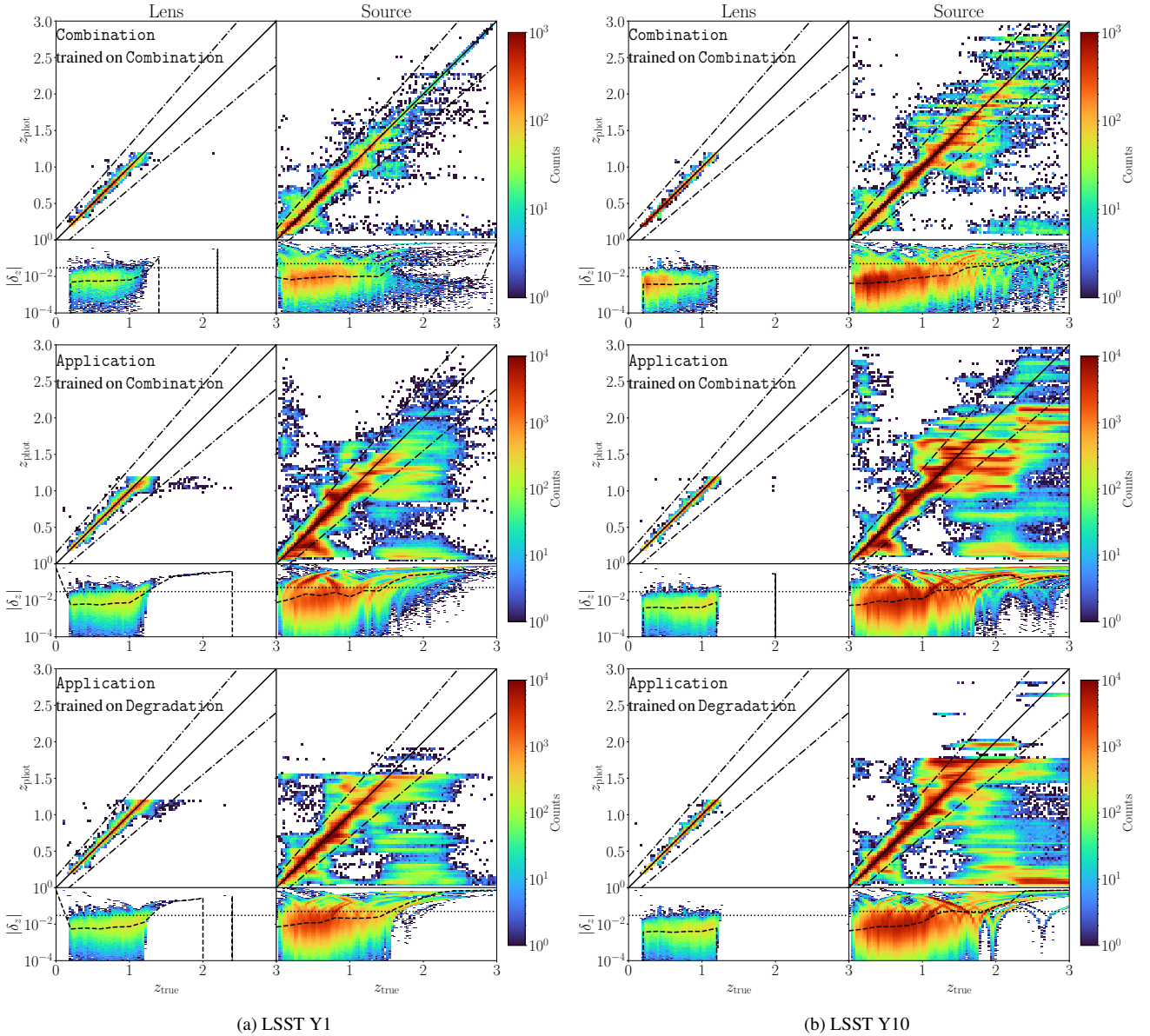


**Figure 9.** Direct visual comparison of  $z_{\text{phot}}$  versus  $z_{\text{true}}$  for the baseline experiment: LSST Y1 (left) and Y10 (right). From top to bottom, each row corresponds to (i) the self-trained Combination dataset utilised as a fully representative benchmark (ii) the Application dataset trained on the augmented Combination dataset; and (iii) the Application dataset trained the Degradation dataset without data augmentation. For every row, the upper panels show two-to-one dimensional histograms for the lens (left) and source (right) samples, where the colour scale represents galaxy counts. The solid black line marks the ideal one-to-one relation  $z_{\text{phot}} = z_{\text{true}}$ , and the dot-dashed lines indicate the outlier threshold  $\delta_z = 0.15$ . The lower panels show the scaled bias  $\delta_z$  as a function of  $z_{\text{true}}$  for lens (left) and source (right) galaxies. The dashed black line denotes the median scaled bias  $\bar{\delta}_z$ , while the dotted lines represent the LSST DESC SRD accuracy requirements of 0.02 for the lens sample and 0.03 for the source sample.

bias, resulting in a non-catastrophic normalised PIT histogram. This observation aligns with the reduction in catastrophic failure rates shown in Figure 8, highlighting that augmentation effectively re-stores missing information in the training dataset.

In the LSST Y10 scenario, the reduction in divergence loss for low-redshift galaxies remains pronounced, by up to a factor of  $\sim 2$  around  $z_{\text{true}} \sim 1.5$ , reflecting improved conditional-density modelling. At higher redshifts, however, only modest gains are seen. This is partly because the deeper spectroscopic Degradation datasets expected for LSST Y10 analysis already enhance the conditional-density estimates for high-redshift galaxies even without augmentation. Additionally, increasingly severe SED mismatches between the

Augmentation and Application datasets for faint, high-redshift galaxies limit further improvements. Nevertheless, data augmentation still reduces the scatter in photometric-redshift performance arising from variations in the spectroscopic selection function.

#### 5.4 Limitations and future work

One significant limitation of data augmentation for photometric-redshift estimation is that the accuracy for galaxies at higher redshifts ( $z_{\text{true}} \geq 1.5$ ) remains contingent upon the fidelity of the SED models in the mock catalogues even though our SOM-based weighted sample can largely align the distributions of galaxies in SED space.

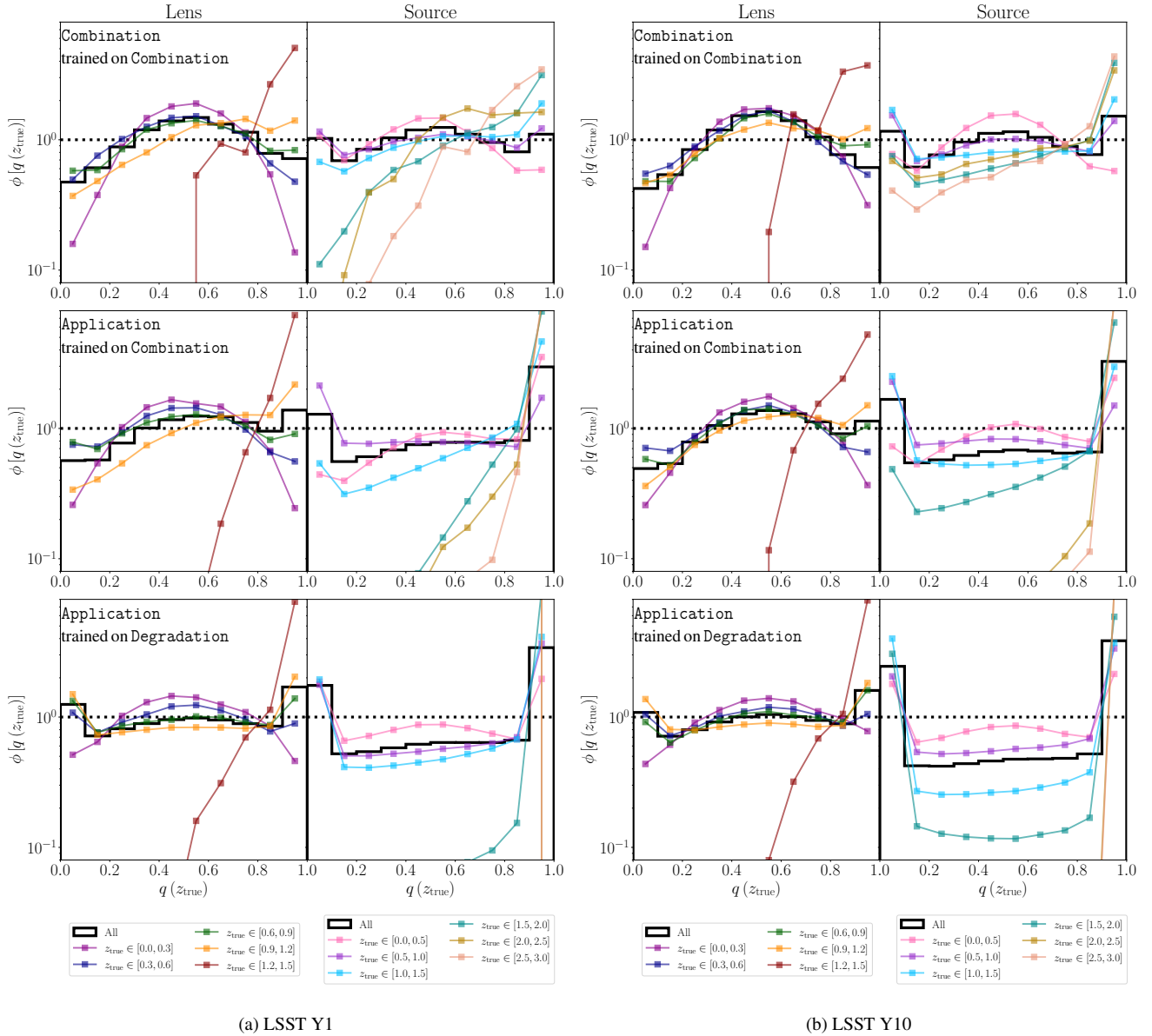


**Figure 10.** Normalised PIT histograms for LSST Y1 (left panel) and Y10 (right panel) are depicted, under the baseline experiment. In each panel, the left subplots show lens samples, while the right subplots present source samples. The black solid lines represent the normalised PIT histogram of the whole sample, whereas the coloured solid lines illustrate the histograms for tomographic bins defined by  $z_{\text{true}}$ , with 10 bins distributed within  $[0.0, 3.0]$ , spaced at intervals of 0.3. The upper row corresponds to the self-trained Combination dataset, which shows idealistic results with fully representative training; the second row relates to the Application dataset trained on the augmented Combination dataset; and the bottom row illustrates the Application dataset trained on the Degradation dataset without data augmentation.

This shortcoming can be further alleviated by recalibrating the auto-differentiable or semi-analytic SED models against early LSST science observations, and by adopting a composite strategy that combines multiple simulations (e.g. Cardinal; To et al. 2024 and SKiLLS; Li et al. 2023b), or even Stellar Population Synthesis (SPS) based mock galaxy SEDs using tools like GalSBI (Fischbacher et al. 2025; Tortorelli et al. 2025) or pop-cosmos (Alsing et al. 2024; Thorp et al. 2024, 2025), to achieve thorough coverage of the SOM space, thereby fully overlapping in the multi-dimensional colour-magnitude volume. By leveraging SOM-based resampling, these comprehensive datasets can then be dynamically matched to observed photometry, offering a robust framework to mitigate residual discrepancies be-

tween simulations and real observations, particularly for faint, high-redshift populations.

Although mock catalogues such as OpenUniverse2024 and CosmoDC2 produce realistic galaxy properties, our analysis currently neglects pixel-level observational artefacts. Future work should incorporate forward-imaging simulations (Troxel et al. 2023), for example employing imSim (Connolly et al. 2014) and GalSim (Rowe et al. 2015), to better capture systematics such as variable survey depth (Leistedt et al. 2016; Johnston et al. 2021; Yan et al. 2025), point-source contamination (Kuijken et al. 2015), and imperfect deblending of faint neighbouring sources (Liang et al. 2025). These enhancements will enable a more realistic characterisation of photometric noise and selection biases, which is essential to ensure that



data-augmentation techniques remain robust against the complexities inherent in real observational datasets.

Our controlled-degradation procedure provides only an approximation to the realistic spectroscopic samples anticipated for LSST cosmological analyses, since the distributions of magnitude and redshift limits will not be uniform across different surveys. Future work should therefore develop more comprehensive and physically motivated definitions of the spectroscopic selection function. Nonetheless, our approach furnishes a systematic framework for propagating selection-function effects into end-to-end photometric-redshift estimates. In practice, numerous spectroscopic surveys (e.g., DESI, PFS, and 4MOST), alongside deep narrow-band imaging programmes (e.g., COSMOS, PAUS, and J-PAS), will be integrated to optimise completeness and diversity within the multi-dimensional colour-magnitude space. Under this multi-survey paradigm, controlled degradation remains a powerful tool: by selectively omitting or reweighting galaxy subsets from individual datasets, we can map the impact of incomplete spectroscopic coverage onto photometric redshifts, thereby enabling a rigorous characterisation of selection-induced uncertainties.

In addition, as discussed in Section 3, our SOM-based data augmentation improves upon the simplified colour-magnitude-redshift boundaries used in Moskowitz et al. (2024) by providing a direct visualisation of the high-dimensional colour-magnitude manifold, thereby streamlining the identification of regions lacking spectroscopic coverage and optimising augmentation efficiency. Nonetheless, every dimensionality-reduction algorithm inevitably distorts the intrinsic topology. Future research will investigate cutting-edge techniques like Uniform Manifold Approximation and Projection (UMAP; McInnes et al. 2018) and  $t$ -distributed Stochastic Neighbour Embedding ( $t$ -SNE; van der Maaten & Hintón 2008), aiming to improve augmentation fidelity. Moreover, more sophisticated and adaptable augmentation criteria can be defined within the joint colour-magnitude-redshift space, providing ample scope for further investigation.

A qualitative comparison with the approach utilised in Moskowitz et al. (2024) proves to be insightful. In that work, photometric redshifts were trained on a combination of currently available spectroscopic samples – analogous to our LSST-Y1-like Degradation datasets – but applied to an LSST-Y10 GoD sample, like our LSST Y10 Application datasets. Consequently, the level of missing spectroscopic information is considerably more significant than in our framework, where we anticipate broader spectroscopic coverage for Y10 analyses, though it remains anticipated. In Moskowitz et al. (2024), the global photometric-redshift metrics, such as biases, outlier fractions, and catastrophic rates, are reduced by a factor of  $\sim 2$  when averaged over the full photometric sample. By contrast, in our analysis, these global statistics show only modest improvement, as they are dominated by low-redshift galaxies with already high spectroscopic completeness. Nevertheless, our augmentation still yields clear benefits for the high-redshift population. Taken together, the two configurations represent complementary scenarios: when the training sample is severely incomplete at the depth of the photometric data, augmentation improves overall performance; when the training sample is already broadly representative, the gains are concentrated at the faint, high-redshift end.

Given the differences between the mock catalogues and the varying photometric and spectroscopic selection functions adopted in this work and in Moskowitz et al. (2024), a direct quantitative comparison is not straightforward. To enable a more rigorous assessment, we are actively analysing observational datasets from the *Rubin* Data

Preview 1 (DP1<sup>23</sup>, NSF-DOE Vera C. Rubin Observatory 2025), which provides catalogue products over seven  $\sim 1\text{deg}^2$  fields for rigorous photometric-redshift validation. These analyses will benchmark our SOM-based augmentation against established methods – both template-fitting and machine-learning – to demonstrate its real-world efficacy. Further comparison using identical mock catalogues will enable careful evaluation of multiple augmentation strategies. The DP1 results will directly inform the integration of both colour-magnitude-redshift and SOM-based data augmentation workflows into the LSST DESC software ecosystem, with particular emphasis on the RAIL platform, thereby substantially enhancing photometric-redshift precision and robustness for Stage-IV cosmological studies.

Ultimately, this work has focused on constructing photometric and spectroscopic datasets and validating the efficacy of the SOM-based data-augmentation technique for photometric-redshift estimation. In both Y1 and Y10 scenarios, the reduction of biases – and in particular the significant decrease in catastrophic failure rates – can substantially mitigate contamination when defining tomographic bins from photometric-redshift estimates, thereby supporting the accurate calibration of ensemble redshift distributions. Building on this foundation, our forthcoming work will extend the framework to optimise tomographic binning strategies for both lens and source samples, following approaches discussed in the literature Zuntz et al. (2021); Moskowitz et al. (2023), as well as to advance the calibration of ensemble redshift distributions. Leveraging the representative training of photometric redshifts and the improved performance achieved in both point estimates and conditional-density modelling, we will then enhance the calibration of ensemble redshift distributions by combining well-behaved conditional PDFs with SOM-based direct calibration (Buchs et al. 2019; Wright et al. 2020, 2025a). This integrated approach aims to satisfy the stringent precision requirements of LSST cosmological analyses, particularly for weak gravitational lensing and large-scale structure studies. Full details will be presented in the accompanying paper (Zhang et al., in preparation).

## 6 CONCLUSIONS

In this study, building off the training sample augmentation technique originally introduced in (Moskowitz et al. 2024), we have developed, implemented and validated a SOM-based data-augmentation framework to improve the accuracy and robustness of photometric-redshift estimation. Starting from two independent mock catalogues – OpenUniverse2024 as a proxy for realistic LSST observations and CosmoDC2 for targeted augmentation – we conducted 501 experiments to generate photometric and spectroscopic datasets under both Y1 and Y10 survey depths.

We first constructed the Application datasets by applying LSST-like photometric errors, shear-noise and the DESC GoD selection to OpenUniverse2024, then trained a SOM on these samples to compress the high-dimensional colour-magnitude space into a two-dimensional grid of cells. Realistic spectroscopic Degradation datasets were produced by sampling this photometric population with magnitude, redshift and colour cuts, plus a logistic function of spectroscopic success rates, and by merging multiple independent realisations to emulate heterogeneous survey compilation.

To compensate for under-sampling in the degraded spectroscopic

<sup>23</sup> <https://dp1.lsst.io>

datasets, we used the CosmoDC2 catalogues with the same photometric pipeline to map each galaxy onto the pre-trained SOM. We applied cell-specific weights to harmonise their overall distributions in SOM space with the photometric Application datasets. We then employed adaptive augmentation by targeting SOM cells that were unoccupied in the Degradation datasets or where galaxies exceeded spectroscopic magnitude or redshift limits, subsequently adding suitably weighted mock galaxies until the proportion of augmented samples to degraded ones matched the deficit of occupied cells.

Using FlexZBoost, a conditional-density machine-learning estimator, we trained photometric-redshift models on the Combination datasets, formed by merging the Degradation and Augmentation catalogues. We quantified point-estimate accuracy via the median scaled bias, NMAD scatter, outlier fraction and catastrophic-failure rate for both lens and source samples, and assessed full PDF fidelity through the divergence loss of the normalised PIT histograms. By benchmarking models trained with and without augmentation against the fully representative self-training reference, we have demonstrated the robustness of our approach and the clear efficacy of SOM-based data augmentation.

Across both Y1 and Y10 scenarios, the lens sample achieves median absolute scaled biases  $|\delta|_z \sim 0.005$ , comfortably within LSST DESC requirements even without augmentation—demonstrating the precision attainable for bright galaxies. For source galaxies at  $z_{\text{true}} \lesssim 1.5$ , we likewise satisfy the science-requirement thresholds. Whilst performance declines at  $z_{\text{true}} \gtrsim 1.5$ , training on the Combination datasets with SOM-based augmentation reduces the average bias and catastrophic failure rate by up to a factor of two, and enhances conditional-PDF modelling, as evidenced by markedly lower divergence losses. Importantly, the reduced scatter across independent realisations shows that augmentation renders photometric-redshift performance largely insensitive to variations in the spectroscopic selection function.

These results demonstrate that SOM-based data augmentation robustly identify the SED space without representative spectroscopic samples and compensates for spectroscopic incompleteness and mitigates SED mismatches, yielding significantly more accurate and reliable photometric-redshift estimates. Such improvements are essential for LSST cosmological and galaxy-evolution analyses, enabling precision measurements of weak gravitational lensing, large-scale structure and the formation history of billions of galaxies across cosmic time.

## CONTRIBUTION STATEMENTS

Y.-H. Z. conceptualised and directed the research, developed the methodologies, conducted the formal analysis – which encompassed dataset construction, photometric-redshift modelling, and evaluation of the effectiveness of the SOM-based data-augmentation technique – and also authored the majority of the manuscript.

J. Z. supervised the work, and contributed conceptually to methodology development, formal analysis, and scientific validation, and also reviewed and refined the manuscript.

I. M. established the data augmentation framework, offered insights on dataset construction and photometric redshift modelling, provided necessary scripts to facilitate the formal analysis, and also reviewed and commented on the manuscript.

E. G. contributed to designing the conceptual framework, advised on dataset construction and photometric redshift modelling, deliv-

ered crucial feedback for scientific validation, and reviewed and commented on the manuscript.

K. K. co-supervised the work, offering guidance on methodology development, formal analysis, and scientific validation, in addition to reviewing and providing feedback on the manuscript.

M. A. proposed refinements for the construction of spectroscopic datasets, advised on the application of the SOM technique, and also reviewed and commented on the manuscript.

H. H. offered insights into the discussion of the scientific findings, emphasised potential areas for future enhancements, and also reviewed and provided feedback on the draft.

Z. Y. assisted in employing the SOM technique, advising on software configuration and scientific validation, and was actively involved in implementing SOM-based data augmentation for the RAIL platform, in addition to reviewing and providing feedback on the manuscript.

A. M. and T. Z. are DESC builders and key developers of the RAIL platform, which is crucial to this work.

## ACKNOWLEDGEMENTS

This manuscript has been internally reviewed by the LSST DESC. The authors express their gratitude to Catherine Heymans and Nora Elisa Chisari for their contribution as members of the DESC publication review committee, whose insightful comments and suggestions enhanced the quality of this paper.

This study extensively utilised publicly available software, including NumPy (Harris et al. 2020), SciPy (Virtanen et al. 2020), and Matplotlib (Hunter 2007), as well as the DESC softwares, particularly RAIL platform, including implementation of Somoclu and FlexZBoost, which were instrumental to this work.

Y.-H. Z. acknowledges support from the UK Research and Innovation (UKRI) Science and Technology Facilities Council (STFC) studentship, the Edinburgh–Leiden joint studentship awarded by the University of Edinburgh and Leiden University, and the STFC travel fund for UK participation in LSST (grant ST/X001334/1).

J. Z. acknowledges the support by STFC funding for UK participation in LSST, through grant ST/X001334/1.

I. M. and E.G. acknowledge support from the U.S. Department of Energy, Office of Science, Office of High Energy Physics Cosmic Frontier Research program under Award Number DE-SC0010008.

M. A. receives support from the UK STFC through grant number ST/Y002652/1, as well as from the Royal Society via grant numbers RGS2222268 and ICAR1231094.

T. Z. is supported by Schmidt Sciences.

The DESC acknowledges ongoing support from the Institut National de Physique Nucléaire et de Physique des Particules in France; the Science & Technology Facilities Council in the United Kingdom; and the Department of Energy and the LSST Discovery Alliance in the United States. DESC uses resources of the IN2P3 Computing Center (CC-IN2P3–Lyon/Villeurbanne - France) funded by the Centre National de la Recherche Scientifique; the National Energy Research Scientific Computing Center, a DOE Office of Science User Facility supported by the Office of Science of the U.S. Department of Energy under Contract No. DE-AC02-05CH11231; STFC DiRAC HPC Facilities, funded by UK BEIS National E-infrastructure capital grants; and the UK particle physics grid, supported by the GridPP Collaboration. This work was performed in part under DOE Contract DE-AC02-76SF00515.

## DATA AVAILABILITY

All scripts associated with this study are publicly available in the GitHub repository [SOMZCloud](https://github.com/SOMZCloud). The generated datasets and accompanying products – including photometric redshift estimates – have been deposited in the LSST DESC Community File System (CFS) at the National Energy Research Scientific Computing Center (NERSC<sup>24</sup>).

## REFERENCES

- Abbott T. M. C., et al., 2022, *Phys. Rev. D*, **105**, 023520
- Akeson R., et al., 2019, *arXiv e-prints*, p. [arXiv:1902.05569](https://arxiv.org/abs/1902.05569)
- Alarcon A., Hearin A. P., Becker M. R., Chaves-Montero J., 2023, *MNRAS*, **518**, 562
- Almosallam I. A., Jarvis M. J., Roberts S. J., 2016, *MNRAS*, **462**, 726
- Alsing J., Thorp S., Deger S., Peiris H. V., Leistedt B., Mortlock D., Leja J., 2024, *ApJS*, **274**, 12
- Amon A., et al., 2022, *Phys. Rev. D*, **105**, 023514
- Arnouts S., Cristiani S., Moscardini L., Matarrese S., Lucchin F., Fontana A., Giallongo E., 1999, *MNRAS*, **310**, 540
- Asgari M., et al., 2021, *A&A*, **645**, A104
- Autenrieth M., Wright A. H., Trotta R., van Dyk D. A., Stenning D. C., Joachimi B., 2024, *MNRAS*, **534**, 3808
- Bartelmann M., Schneider P., 2001, *Phys. Rep.*, **340**, 291
- Bechtol K., et al., 2025, *arXiv e-prints*, p. [arXiv:2501.05739](https://arxiv.org/abs/2501.05739)
- Behroozi P. S., Wechsler R. H., Conroy C., 2013, *ApJ*, **770**, 57
- Behroozi P., Wechsler R. H., Hearin A. P., Conroy C., 2019, *MNRAS*, **488**, 3143
- Benítez N., 2000, *ApJ*, **536**, 571
- Benítez N., et al., 2015, in Cenarro A. J., Figueras F., Hernández-Monteagudo C., Trujillo Bueno J., Valdivielso L., eds, *Highlights of Spanish Astrophysics VIII*. pp 148–153
- Benson A. J., Borgani S., De Lucia G., Boylan-Kolchin M., Monaco P., 2012, *MNRAS*, **419**, 3590
- Bernstein G. M., Jarvis M., 2002, *AJ*, **123**, 583
- Besuner R., et al., 2025, *arXiv e-prints*, p. [arXiv:2503.07923](https://arxiv.org/abs/2503.07923)
- Bordoloi R., et al., 2012, *MNRAS*, **421**, 1671
- Bouwens R., Illingworth G., Oesch P., Stefanon M., Naidu R., van Leeuwen I., Magee D., 2023, *MNRAS*, **523**, 1009
- Brammer G. B., van Dokkum P. G., Coppi P., 2008, *ApJ*, **686**, 1503
- Brinchmann J., et al., 2017, *A&A*, **608**, A3
- Buchs R., et al., 2019, *MNRAS*, **489**, 820
- Burgett W., et al., 2024, in Marshall H. K., Spyromilio J., Usuda T., eds, *Society of Photo-Optical Instrumentation Engineers (SPIE) Conference Series Vol. 13094, Ground-based and Airborne Telescopes X*. p. 1309417, doi:[10.1117/12.3020733](https://doi.org/10.1117/12.3020733)
- Cagliari M. S., et al., 2024, *A&A*, **689**, A166
- Cavuoti S., Brescia M., Longo G., Mercurio A., 2012, *A&A*, **546**, A13
- Cavuoti S., Amaro V., Brescia M., Vellucci C., Tortora C., Longo G., 2017, *MNRAS*, **465**, 1959
- Chang C., et al., 2013, *MNRAS*, **434**, 2121
- Chen T., Guestrin C., 2016, *arXiv e-prints*, p. [arXiv:1603.02754](https://arxiv.org/abs/1603.02754)
- Coe D., Benítez N., Sánchez S. F., Jee M., Bouwens R., Ford H., 2006, *AJ*, **132**, 926
- Colless M., et al., 2001, *MNRAS*, **328**, 1039
- Collister A. A., Lahav O., 2004, *PASP*, **116**, 345
- Connolly A. J., et al., 2014, in Angeli G. Z., Dierickx P., eds, *Society of Photo-Optical Instrumentation Engineers (SPIE) Conference Series Vol. 9150, Modeling, Systems Engineering, and Project Management for Astronomy VI*. p. 915014, doi:[10.1117/12.2054953](https://doi.org/10.1117/12.2054953)
- Conselice C. J., 2014, *ARA&A*, **52**, 291
- Crenshaw J. F., Kalmbach J. B., Gagliano A., Yan Z., Connolly A. J., Malz A. I., Schmidt S. J., The LSST Dark Energy Science Collaboration 2024, *AJ*, **168**, 80
- DESI Collaboration et al., 2024, *AJ*, **167**, 62
- Dahlen T., et al., 2013, *ApJ*, **775**, 93
- Dalal R., et al., 2023, *Phys. Rev. D*, **108**, 123519
- Dalmaso N., Pospisil T., Lee A. B., Izbicki R., Freeman P. E., Malz A. I., 2020, *Astronomy and Computing*, **30**, 100362
- Dark Energy Survey and Kilo-Degree Survey Collaboration et al., 2023, *The Open Journal of Astrophysics*, **6**, 36
- Davidzon I., et al., 2017, *A&A*, **605**, A70
- Daza-Perilla I. V., et al., 2025, *A&A*, **693**, A102
- Driver S. P., et al., 2011, *MNRAS*, **413**, 971
- Duncan K. J., et al., 2019, *A&A*, **622**, A3
- Dvornik A., et al., 2023, *A&A*, **675**, A189
- Eisenstein D. J., et al., 2005, *ApJ*, **633**, 560
- Euclid Collaboration et al., 2025, *A&A*, **697**, A1
- Feldmann R., et al., 2006, *MNRAS*, **372**, 565
- Finkelstein S. L., et al., 2015, *ApJ*, **810**, 71
- Fischbacher S., Kacprzak T., Tortorelli L., Moser B., Refregier A., Gebhardt P., Gruen D., 2025, *J. Cosmology Astropart. Phys.*, **2025**, 007
- Fotopoulou S., et al., 2012, *ApJS*, **198**, 1
- Freeman P. E., Izbicki R., Lee A. B., 2017, *MNRAS*, **468**, 4556
- Gardner J. P., et al., 2006, *Space Sci. Rev.*, **123**, 485
- Gong Y., et al., 2019, *ApJ*, **883**, 203
- Gris P., Awan H., Becker M. R., Lin H., Gawiser E., Jha S. W., The LSST Dark Energy Science Collaboration 2024, *ApJS*, **275**, 21
- Guzzo L., et al., 2014, *A&A*, **566**, A108
- Habib S., et al., 2016, *New Astron.*, **42**, 49
- Harris C. R., et al., 2020, *Nature*, **585**, 357
- Hartley W. G., et al., 2020, *MNRAS*, **496**, 4769
- Hearin A., Korytov D., Kovacs E., Benson A., Aung H., Bradshaw C., Campbell D., LSST Dark Energy Science Collaboration 2020, *MNRAS*, **495**, 5040
- Hearin A. P., Chaves-Montero J., Becker M. R., Alarcon A., 2021, *The Open Journal of Astrophysics*, **4**, 7
- Hearin A. P., Chaves-Montero J., Alarcon A., Becker M. R., Benson A., 2023, *MNRAS*, **521**, 1741
- Heitmann K., et al., 2019, *ApJS*, **245**, 16
- Heymans C., et al., 2021, *A&A*, **646**, A140
- Hildebrandt H., et al., 2010, *A&A*, **523**, A31
- Hunter J. D., 2007, *Computing in Science and Engineering*, **9**, 90
- Ilbert O., et al., 2006, *A&A*, **457**, 841
- Ivezić Z., et al., 2019, *ApJ*, **873**, 111
- Izbicki R., Lee A. B., 2017, *Electronic Journal of Statistics*, **11**, 2800
- Jin S., et al., 2024, *MNRAS*, **530**, 2688
- Johnston H., et al., 2021, *A&A*, **648**, A98
- Kaiser N., 1998, *ApJ*, **498**, 26
- Kennicutt Jr. R. C., 1998, *ApJ*, **498**, 541
- Kilbinger M., 2015, *Reports on Progress in Physics*, **78**, 086901
- Koo D. C., 1985, *AJ*, **90**, 418
- Kormendy J., Ho L. C., 2013, *ARA&A*, **51**, 511
- Korytov D., et al., 2019, *ApJS*, **245**, 26
- Kovacs E., et al., 2022, *The Open Journal of Astrophysics*, **5**, 1
- Kuijken K., et al., 2015, *MNRAS*, **454**, 3500
- LSST Dark Energy Science Collaboration et al., 2018, *arXiv e-prints*, p. [arXiv:1809.01669](https://arxiv.org/abs/1809.01669)
- LSST Dark Energy Science Collaboration et al., 2021, *ApJS*, **253**, 31
- LSST Science Collaboration et al., 2009, *arXiv e-prints*, p. [arXiv:0912.0201](https://arxiv.org/abs/0912.0201)
- Leistedt B., Hogg D. W., 2017, *ApJ*, **838**, 5
- Leistedt B., et al., 2016, *ApJS*, **226**, 24
- Li X., et al., 2022, *PASJ*, **74**, 421
- Li X., et al., 2023a, *Phys. Rev. D*, **108**, 123518
- Li S.-S., et al., 2023b, *A&A*, **670**, A100
- Li S.-S., et al., 2023c, *A&A*, **679**, A133
- Liang S., Adari P., von der Linden A., 2025, *arXiv e-prints*, p. [arXiv:2503.16680](https://arxiv.org/abs/2503.16680)
- Lilly S. J., et al., 2007, *ApJS*, **172**, 70

<sup>24</sup> <https://www.nersc.gov>

- Loh E. D., Spillar E. J., 1986, *ApJ*, **303**, 154
- Mandelbaum R., 2018, *ARA&A*, **56**, 393
- Mao Y.-Y., et al., 2018, *ApJS*, **234**, 36
- Masters D., et al., 2015, *ApJ*, **813**, 53
- McInnes L., Healy J., Melville J., 2018, *arXiv e-prints*, p. [arXiv:1802.03426](#)
- Miyatake H., et al., 2023, *Phys. Rev. D*, **108**, 123517
- Moretti C., Autenrieth M., Serra R., Trotta R., van Dyk D. A., Mesinger A., 2025, *The Open Journal of Astrophysics*, **8**, 50
- Moskowitz I., Gawiser E., Bault A., Broussard A., Newman J. A., Zuntz J., LSST Dark Energy Science Collaboration 2023, *ApJ*, **950**, 49
- Moskowitz I., Gawiser E., Crenshaw J. F., Andrews B. H., Malz A. I., Schmidt S., LSST Dark Energy Science Collaboration 2024, *ApJ*, **967**, L6
- NSF-DOE Vera C. Rubin Observatory 2025, Legacy Survey of Space and Time Data Preview 1 [Data set], [doi:10.71929/RUBIN/2570308](#), <https://www.osti.gov/servlets/purl/2570308>
- Newman J. A., Gruen D., 2022, *ARA&A*, **60**, 363
- Newman J. A., et al., 2013, *ApJS*, **208**, 5
- OpenUniverse et al., 2025, *arXiv e-prints*, p. [arXiv:2501.05632](#)
- Padovani P., Cirasuolo M., 2023, *Contemporary Physics*, **64**, 47
- Peebles P. J. E., 1980, *The large-scale structure of the universe*. Princeton University Press
- Perlmutter S., et al., 1999, *ApJ*, **517**, 565
- Porredon A., et al., 2021, *Phys. Rev. D*, **103**, 043503
- Raichoor A., et al., 2023, *AJ*, **165**, 126
- Revsbech E. A., Trotta R., van Dyk D. A., 2018, *MNRAS*, **473**, 3969
- Riess A. G., et al., 1998, *AJ*, **116**, 1009
- Rowe B. T. P., et al., 2015, *Astronomy and Computing*, **10**, 121
- Sadeh I., Abdalla F. B., Lahav O., 2016, *PASP*, **128**, 104502
- Schechter P., 1976, *ApJ*, **203**, 297
- Schlegel D. J., et al., 2022a, *arXiv e-prints*, p. [arXiv:2209.03585](#)
- Schlegel D. J., et al., 2022b, *arXiv e-prints*, p. [arXiv:2209.04322](#)
- Schmidt S. J., et al., 2020, *MNRAS*, **499**, 1587
- Secco L. F., et al., 2022, *Phys. Rev. D*, **105**, 023515
- Shibuya T., Ouchi M., Harikane Y., 2015, *ApJS*, **219**, 15
- Shuntov M., et al., 2022, *A&A*, **664**, A61
- Spergel D., et al., 2015, *arXiv e-prints*, p. [arXiv:1503.03757](#)
- Springel V., Frenk C. S., White S. D. M., 2006, *Nature*, **440**, 1137
- Stözlner B., et al., 2025, *arXiv e-prints*, p. [arXiv:2503.19442](#)
- Sugiyama S., et al., 2023, *Phys. Rev. D*, **108**, 123521
- Takada M., et al., 2014, *PASJ*, **66**, R1
- Tanaka M., et al., 2018, *PASJ*, **70**, S9
- The RAIL Team et al., 2025, *arXiv e-prints*, p. [arXiv:2505.02928](#)
- Thorp S., Alsing J., Peiris H. V., Deger S., Mortlock D. J., Leistedt B., Leja J., Loureiro A., 2024, *ApJ*, **975**, 145
- Thorp S., et al., 2025, *arXiv e-prints*, p. [arXiv:2506.12122](#)
- To C.-H., et al., 2024, *ApJ*, **961**, 59
- Tortorelli L., Fischbacher S., Grün D., Refregier A., Bellstedt S., Robotham A. S. G., Kacprzak T., 2025, *arXiv e-prints*, p. [arXiv:2505.21610](#)
- Tremonti C. A., et al., 2004, *ApJ*, **613**, 898
- Troxel M. A., et al., 2023, *MNRAS*, **522**, 2801
- Tyson J. A., Valdes F., Wenk R. A., 1990, *ApJ*, **349**, L1
- Virtanen P., et al., 2020, *Nature Methods*, **17**, 261
- Walcher C. J., et al., 2016, in Peck A. B., Seaman R. L., Benn C. R., eds, *Society of Photo-Optical Instrumentation Engineers (SPIE) Conference Series Vol. 9910, Observatory Operations: Strategies, Processes, and Systems VI*. p. 99101N, [doi:10.1117/12.2233187](#)
- Weaver J. R., et al., 2022, *ApJS*, **258**, 11
- Wechsler R. H., Tinker J. L., 2018, *ARA&A*, **56**, 435
- Wittek P., Chao Gao S., Lim I. S., Zhao L., 2013, *arXiv e-prints*, p. [arXiv:1305.1422](#)
- Wright A. H., Hildebrandt H., van den Busch J. L., Heymans C., 2020, *A&A*, **637**, A100
- Wright A. H., et al., 2024, *A&A*, **686**, A170
- Wright A. H., et al., 2025a, *arXiv e-prints*, p. [arXiv:2503.19440](#)
- Wright A. H., et al., 2025b, *arXiv e-prints*, p. [arXiv:2503.19441](#)
- Yan Z., et al., 2025, *A&A*, **694**, A259
- Yang G., et al., 2014, *ApJS*, **215**, 27
- York D. G., et al., 2000, *AJ*, **120**, 1579
- Zhao C., et al., 2024, *arXiv e-prints*, p. [arXiv:2411.07970](#)
- Zuntz J., et al., 2021, *The Open Journal of Astrophysics*, **4**, 13
- van den Busch J. L., et al., 2020, *A&A*, **642**, A200
- van der Maaten L., Hinton G., 2008, *Journal of Machine Learning Research*, **9**, 2579

This paper has been typeset from a  $\text{\LaTeX}$  file prepared by the author.